Forschungszentrum Karlsruhe
in der Helmholtz-Gemeinschaft

Wissenschaftliche Berichte
FZKA 7390

Charge-Induced Tunable Magnetic Properties in Transition Metal Alloys

S. Ghosh

Institut für Nanotechnologie

März 2008

Forschungszentrum Karlsruhe

in der Helmholtz-Gemeinschaft

Wissenschaftliche Berichte

FZKA 7390

Charge-Induced Tunable Magnetic Properties in Transition Metal Alloys

Sadhan Ghosh

Institut für Nanotechnologie

Von der Naturwissenschaftlich–Technischen Fakultät II

- Physik und Mechatronik -

der Universität des Saarlandes genehmigte Dissertation

Forschungszentrum Karlsruhe GmbH, Karlsruhe

2008

Forschungszentrum Karlsruhe GmbH
Postfach 3640, 76021 Karlsruhe

Mitglied der Hermann von Helmholtz-Gemeinschaft
Deutscher Forschungszentren (HGF)

ISSN 0947-8620

urn:nbn:de:0005-073900

Charge-Induced Tunable Magnetic Properties in Transition Metal Alloys

---

Mittels elektrischer Ladungen durchstimmbare magnetische Eigenschaften in Übergangsmetalllegierungen

Zur Erlangung des akademischen Grades eines

DOKTORS DER INGENIEURWISSENSCHAFTEN

von der Fakultät für Physik und Mechatronik der

Universität des Saarlandes

genehmigte

DISSERTATION

von

ME-Eng. Sadhan Ghosh

aus Kolkata, Indien

Tag des Kolloquiums: 19.02.2008

Referent: PD Dr. Jörg Weissmüller

Korreferent: Univ.-Prof. Dr. Uwe Hartmann

Abstract

Ferromagnetism in transition metals is fundamentally related to the electronic density of states. Therefore, it is interesting to study how far one can modify the magnetic order of solids by changing their electron density. The approach appears particularly promising in nanostructured materials, since high surface to volume ratio maximizes the effect of local property changes in the space-charge layers at the surface. Here, we explore how far the magnetization of nanoporous transition metal alloys may be modified by polarizing their surfaces against an electrolyte. Though the Thomas-Fermi screening length is around one lattice constant in metals, a significant reversible variation of magnetization and susceptibility for Pd-Ni and Pd-Co alloys has been observed at room temperature during charging of the metal surfaces in an electrolyte. The experimental investigation put forward two possible underlying mechanisms, 1) a direct effect of the modified electron density near the surface on the magnetic moment per atom, and 2) an indirect interaction, where the magnetization is affected by the surface-induced stress in the bulk via magnetoelastic coupling. At the end, it was found that magnetoelastic response effect on its own can explain the experimental observations as electrochemical charging leads to elastic strain or stress in the nanoporous structure.

Deutsche Zusammenfassung

Der Ferromagnetismus in Übergangsmetallen hängt grundlegend von der elektronischen Zustandsdichte ab. Folglich ist es aufschlussreich, zu untersuchen, inwieweit man die magnetische Ordnung von Festkörpern ändern kann, indem man ihre Elektrondichte ändert. Dieser Ansatz erscheint für nanostrukturierte Materialien besonders viel versprechend, da das hohe Verhältnis von Oberfläche zum Volumen die Auswirkungen von lokalen Eigenschaftsänderungen in den Raumladungsschichten an der Oberfläche maximiert. Hier erforschen wir, wie weit die Magnetisierung der nanoporösen Übergangsmetalllegierungen durch die Polarisierung ihrer Oberflächen in einem Elektrolyten geändert werden kann. Obwohl die Thomas-Fermi-Abschirmlänge in Metallen nur etwa eine Gitterkonstante beträgt, ist eine bedeutende reversible Änderung der Magnetisierung und der Suszeptibilität für Palladium-Nickel- und Palladium-Kobalt-Legierungen bei Raumtemperatur beobachtet worden, wenn die Metalloberfläche in einem Elektrolyten aufgeladen wurde. Die experimentelle Untersuchungen legen zwei mögliche zugrundeliegende Mechanismen nahe: 1. der direkte Effekt der nahe der Oberfläche geänderten Elektrondichte auf das magnetische Moment pro Atom und 2. eine indirekte Wechselwirkung, bei der die Magnetisierung durch den von der Oberfläche verursachten Druck im Volumen über magnetoelastische Koppelung beeinflußt wird. Schließlich wurde gezeigt, dass allein die magnetoelastischen Wirkungen die experimentellen Beobachtungen erklären können, weil die elektrochemische Aufladung zu Spannungen und Dehnungen in der nanoporösen Struktur führt.

Zusammenfassung

Mittels elektrischer Ladungen durchstimmbare magnetische Eigenschaften in Übergangsmetalllegierungen

Die Eigenschaften von Nanomaterialien lassen sich nach GLEITER reversibel verändern, wenn sie durch Anlegen einer elektrischen Spannung aus dem Zustand der Ladungsneutralität gebracht werden. Da viele Eigenschaften, z.B. optische, elektrische und magnetische, stark von der elektronischen Zustandsdichte abhängen, könnte dies die Tür zu einer neuen Generation durchstimmbarer Materialien öffnen.

Bei Halbleitern bilden sich im elektrischen Feld an den Grenzflächen Raumladungszonen mit einer Ausdehnung über 10-1000 Gitterparameter. In Metallen erstrecken sich diese Zonen wegen der kleineren Abschirmlänge über wenige Atomdurchmesser, und durch sie hervorgerufene Effekte sind wegen der geringen Zahl betroffener Atome meist nur schwer nachweisbar. Nanostrukturierte Materialien hingegen sind wegen ihres großen Verhältnisses von Oberfläche zu Volumen ideal für Untersuchungen von Eigenschaften, die stark durch Grenzflächen bestimmt sind. 2003 war gezeigt worden, dass elektrische Ladungen – die mit Hilfe einer Gegenelektrode in einem Elektrolyten variiert wurden – in nanoporösen Metall mit der elastischen Grenzflächenspannung auch den Gitterparameter reversibel ändern. Überschussladungen im Metall von etwa 1/10 e^- pro Atom (im Vergleich zu 1/10000 im Halbleiter) bei einer deutlich höheren Zahl von Oberflächenatomen führen zu einem gut messbaren Effekt. Es ist das Thema dieser Arbeit, den Einfluss von Oberflächenladungen auf die Magnetisierung in nanoporösen Metalllegierungen zu untersuchen.

Einem vereinfachten Bändermodell zufolge hängt der Magnetismus der Übergangsmetalle von der elektronische Zustandsdichte im 3d-Band ab: Maximale Magnetisierung ist erreicht, wenn das Band mit der maximalen Zahl ungepaarter Elektronen besetzt ist. Bei weiterer Auffüllung fällt das magnetische Moment wieder ab. So wird ferromagnetisches Nickel paramagnetisch, wenn pro Atom 0.54 Elektronen hinzulegiert werden. Die vorliegende Arbeit geht der Frage nach, inwieweit sich derselbe Effekt auch durch eine oberflächennahe Raumladung erzielen lässt.

Im experimentellen Teil wurden als Modellsysteme verschiedene Zusammensetzungen von Pd-Ni- und Pd-Co-Legierungen untersucht. Zur Probenherstellung wurde mittels Edelgaskondensation ein nanokristallines Pulver synthetisiert, das zu einem lockeren Agglomerat verpresst wurde. Die Legierungszusammensetzung wurde mit energiedispersiver Röntgen-Fluoreszenzanalyse (EDAX) bestimmt. Eine Auswertung der Bragg-Peak-Verbreiterung ergab eine mittlere Korngröße von 6±2 nm. Die Mikrostruktur wurde mittels Raster- und Transmissionselektronenmikroskopie charakterisiert. Hystereseschleifen bei verschiedenen Temperaturen sowie Messungen der Magneti-

sierung nach Abkühlung mit und ohne angelegtes Magnetfeld wurden zur Bestimmung von magnetischen Eigenschaften wie der Curietemperatur vor Kontakt mit dem Elektrolyten durchgeführt.

Wichtig für die Messungen war die Auswahl eines geeigneten Elektrolyten: In 1 M Lithiumperchlorat in Ethylacetat erweisen sich die Pellets als elektrochemisch stabil, und ein Spannungsfenster mit vorwiegend kapazitiver Umladung, d.h. mit einem Minimum an chemischen Reaktionen, konnte gefunden werden. Es wurde eine Mikromesszelle konstruiert, die es ermöglicht, *in-situ* magnetische Messungen unter kontrolliertem elektrochemischen Potential durchzuführen. Als Gegenelektrode diente poröser Kohlenstoff, als Referenzelektrode eine Silber-Silberchloridelektrode. Die Messung der Magnetisierung erfolgte in DC- bzw. AC- Modus, während die Probe im Magnetometer mit einem Potentiostaten kontrolliert und wiederholt umgeladen wurde. Die zyklische Änderung der Magnetisierung wurde mit der Exzessladung Q korreliert, wobei sich zeigt, dass die Magnetisierung reversibel und linear mit Q variiert. Die Amplitude ist abhängig von der Legierungszusammensetzung und weist bei PdNi einen Vorzeichenwechsel auf.

Da die Absorption von Wasserstoff, die durch den nichtwässrigen Elektrolyten ohnehin minimiert ist, zu einem der Beobachtung entgegengesetztem Vorzeichen führen würde, kann eine darauf beruhende Erklärung der Ergebnisse ausgeschlossen werden. Oberflächenoxidation und Adsorptionsprozesse und die entsprechende Beiträge zur Magnetisierungsänderung wurden durch die Wahl des geeigneten Potentialfensters weitgehend vermieden. Da die Steigung $\mathrm{d}M/\mathrm{d}Q$ bei vielen Legierungszusammensetzungen negativ ist, ergibt sich ein Widerspruch zum erläuterten Modell des Auffüllens des 3d-Bandes mit Elektronen, das die Magnetisierung in Pd-Co und nickelreichen Pd-Ni-Legierungen reduzieren sollte. Daher zeigt sich, dass der Großteil der beobachteten Veränderung an den Druckeffekt auf die Kristallite gekoppelt ist, welcher durch die ladungsinduzierten Grenzflächenspannungsänderungen erzeugt wird. Die Wirkung von mechanischem Druck auf das magnetische Moment ist bekannt: Es ändert sich durch die Variation der elektronischen Zustandsdichte aufgrund der Verschiebung der Fermi-Energie. Anhand der bekannten Magnetisierungs-Druck-Koeffizienten wird gezeigt, dass die Amplitude der Änderung des magnetischen Moments sehr gut mit den experimentellen Ergebnissen übereinstimmt und zudem den konzentrationsabhängigen, bei der Pd-Ni-Legierung beobachteten Vorzeichenwechsel erklärt. Das jeweilige beobachtete Vorzeichen der Magnetisierung kann mit der konzentrationsabhängigen Anisotropiekonstanten der Legierung korreliert werden.

In der vorliegenden Arbeit wird also gezeigt, dass magnetische Momente durch elektrochemische Beladung reversibel verändert werden können. Als Hauptursache dafür konnte der inverse magnetostriktive Effekt identifiziert werden, wobei die Druckänderung im Material durch die Ladungsabhängigkeit der elastischen Grenzflächenspannung hervorgerufen wird.

Contents

1 Introduction

1.1 Technological interest in nanomaterials

Nanomaterials are crystalline solids with a grain size of few nanometers [1]. The properties of matter differ considerably when the structure size is reduced from micro to nano size range. A small dimension of the crystallites increases the area of interfaces, therefore a large fraction of atoms – typically more than 10% – locate at the surface [2]. The change in dimension from centimetre to nanometer size increases the surface area and the surface energy to about seven orders of magnitude [3]. Therefore, the properties of the whole material can be different from those of comparable substances with larger structure size.

The current journey of nanomaterials started nearly two decades back, but people are heard to use this material from very old days. Chinese people employed gold nano-particles as a dopant to introduce red colour into their ceramic porcelains more than thousand years ago [4]. It is now being used as catalytic converter for increased surface reactivity in the nanometer scale [5]. Until now various fundamental properties have been studied with the nanocrystalline microstructure and in many cases superior material properties were found compared to coarse grained counter parts. A good combination of strength [6], ductility [7] and wear-resistance [8] has proved them an attractive material for mechanical and defense [9] applications. A simple reason is that the deformation behaviour changes with the reduction of grain size as hard and brittle ceramics tend to be ductile [10] in the nanocrystalline state.

The magnetic properties of nanostcrystalline materials are markedly different from those of the coarse grained structure. When the size of magnetic particles is reduced to a few tens of nanometers, they may exhibit a number of outstanding physical properties, such as increased Curie temperature [11] and a low coercivity [12]. A ferromagnetic material may also turn into superparamagnetic state at reduced dimension in nanometer scale [13]. Electrical resistivity increases with reduction in grain size due to scattering of electrons at the interface boundaries [2]. Self-purification may be an easy option for nanomaterials as impurity and intrinsic material defects can be depleted to the nearby surfaces by thermal annealing [3].

Nanomaterials synthesized into porous structure are of scientific and technological interest because of their increased reactivity not only at the surface, but throughout the bulk [14]. It is seen that porous structure can also be mechanically stronger compared to the bulk [15]. Recently, nanoporous metals immersed in electrolytes have emerged as a new class of material to be used as actuator owing to their ability to change the dimensions with an electric charge [16]. The concept of electrochemical charging in nanoporous structure basically opens a way for exploring tunable material properties in high surface area materials [17].

The demand for this fine scale material is never ending. Scientists around the globe are now making efforts to find the best possible applications. The result is the birth of a new technology, called Nanotechnology. With the aid of this technology it might be possible to transfer drugs in an animal body through nano-tubes or diagnose a disease through nano-robots in medical applications [18]. Nanotechnology is playing an increasing role in solving the world energy crisis through the introduction of fuel cells and battery cells as hydrogen can be effectively stored at the high surface area nanomaterials [19]. It is slowly drawing impact in the growing electronic industries, which has long lasting demands for high speed and long durability tiny product like microprocessors with the ability for better thermal conductivity and heat dissipation capability. In short nanomaterials can be termed as future generation material, whose presence can be visible in different sectors of our society, starting from health to energy, defence to automobile, electronic to entertainment industries and more.

1.2 Motivation of the work

Virtually all materials studied or technologically used today are electrically neutral, i.e. the positive and negative charges are balanced. It has been pointed out [17] that breaking the charge neutrality might expose interesting new science and a potential functional material if the concept is applied to nano-materials whose properties are dominated by extremely large numbers of the surface to volume ratio.

If two semi-infinite crystals are separated by a dielectric medium and potential is applied between them by an external electrical source, one will gain electrons at the expense of the other as shown in Fig. 1.1. If the gap between both crystals is d, the charge density (per unit area), q, transferred from one crystal to the other under the application of applied potential, U is

$$q = \varepsilon\varepsilon_0 \frac{U}{d} \tag{1}$$

where ε is the dielectric constant of the medium separating the two crystals and ε_0 is the dielectric constant of vacuum.

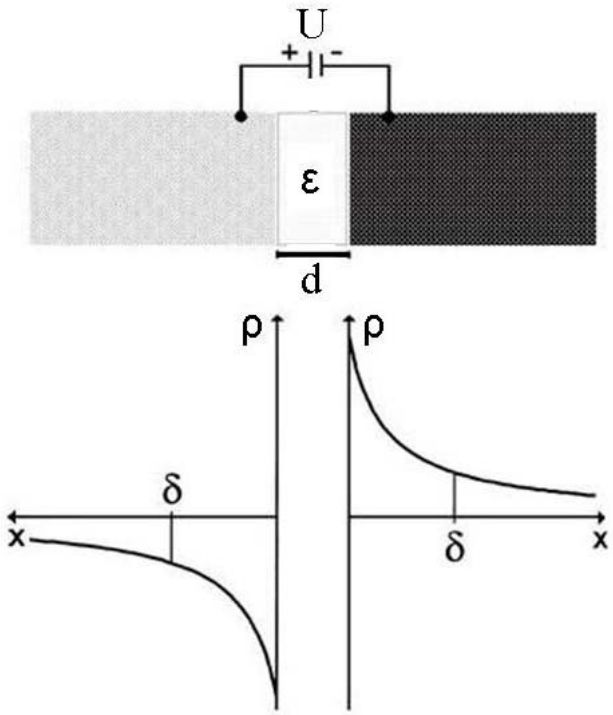

Fig. 1.1: Charge density, ρ in semi-infinite crystals adjacent to an insulating interface (thickness *d*, relative dielectric constant ε) upon applying a voltage *U*. δ: screening length, [17].

The depth of penetration of charge from surface to the interior of a solid is known as screening length. The dimension of the screening length, δ, is estimated to be 10-1000 lattice constants for semiconductors in comparison to one lattice constant in metals. A space charge layer can significantly affect the properties of materials, as evidenced by many applications in semiconductor research and devices, most notably the field-effect transistor where the electron density can be altered with the application of external electric field. The large screening length in semiconductors is a result of the low free charge (extra electrons/holes) carrier density, which carries charge much deeper into the solid. In metals, the induced charge, which is maximum few tenths of electrons per interfacial atom, remains localised to the surface. Therefore, a considerable variation of the surface properties seems

to be possible, and a considerable change in the properties of the whole material in case the material is nanomaterial.

The transfer of charge at the electrode-electrolyte interface is an established fact in electrochemistry. When the wetted surface of the metallic solid is polarised [16, 20] by an external voltage against a counter electrode, it results in storage of large electrical charge at the electrode-electrolyte interface as shown in Fig. 1.2. Large charge densities can be obtained due to the huge capacity of the electrochemical double layer: the distance d as given in Eq. (1) is in the order of atomic dimensions. Furthermore, since the electrolyte can impregnate into the pores of a solid, a complete charging of spongelike structures can easily be achieved.

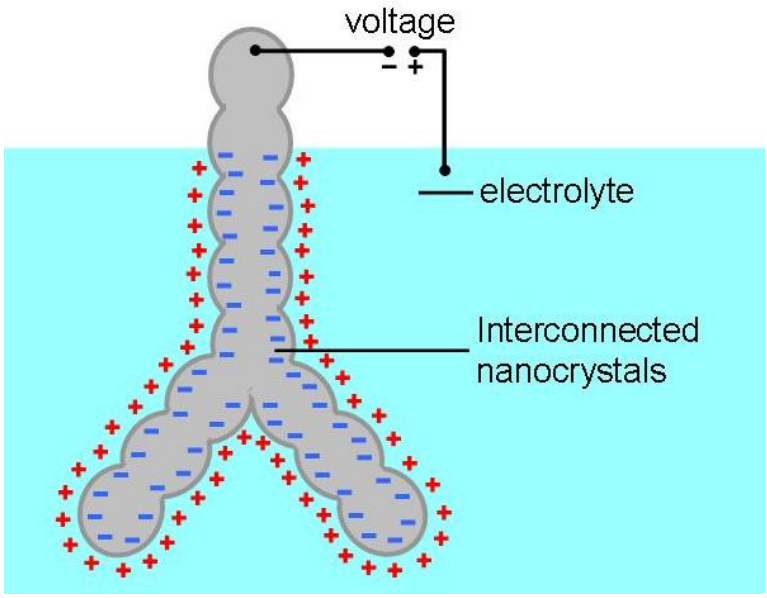

Fig. 1.2: Schematic representation of the space charge layer induced by an electric voltage in an interconnected array of charged nanoparticles immersed in an electrolyte [16].

The application of an electric potential generates an excess charge at the surface of the solid adjacent to the electrolyte and the surface atoms will deviate from charge neutrality. As an example Fig. 1.2 shows the accumulation of negative charges to the surface atoms on the application of negative potential to the crystallites with respect to the electrolyte. As a re-

sult, positive ions from the electrolyte will move towards the metal surface and counterbalance these negatives charges, to maintain the overall charge neutrality of the system. So the interface will resemble to an ideal capacitor of two dissimilar charges. However, in addition to electrostatic charging, chemical processes like the oxidation of the surface might also occur. To distinguish between these two microscopic processes, it is helpful to use a voltammogram, which shows the current that is recorded during a cyclic variation of the applied potential. Since the current can be large during chemical processes, including adsorption, a small and constant current within a particular potential window can be an indication of the region of the least specific adsorption [21, 22] or the Helmholtz double layer regime [20, 21, 23]. The properties of the matter, studied in this capacitive charging potential region are expected to be governed rather by the effect of the excess charges [fig. 1.2] than by the modification of the electrode surface with an adsorbate.

Recently, reversible property changes have become an interest in the context of the capacitive charging near the double layer region. It has been demonstrated that the elastic strain of nano-porous Pt and Au can be varied reversibly with the effective control of charge density at the metal-electrolyte interface [16, 24]. The excess charge density basically changes the interatomic bonding at the surface. For nanomaterials, this results in a considerable change of the lattice parameter. Following the similar concept, the electrical conductivity [25] of nanoporous materials was tuned reversibly through the variation of charge density at the space charge layer.

Similar evidences have been documented for other high-surface area nano-materials, such as carbon nanotubes where strain [26] and optical absorbance [27] were varied reversibly by an applied voltage. The double layer charging leads to a change in valence or conduction band electron density of the semiconductor material. However, little attention has been paid so far to the possibility of changing the magnetic behaviour, e.g. of transition metals, with an extra charge carrier density. The conventional way of changing the magnetic ordering of solids is by changing the temperature or the magnetic field. A similar effect can also be seen during alloying. As an example [28], if Cu is alloyed with Ni, 4s electrons of Cu fills up the empty 3d band of Ni, thus switching ferromagnetic Ni into paramagnetic state at $Cu_{60}Ni_{40}$ when 0.54 holes per atom are completely filled up by Cu electrons as shown in Fig. 1.3.

The loss of ferromagnetism is marked as irreversible change because composition of a material is always fixed at the time of synthesis. Recently, Gleiter *et. al.* [17] proposed that without changing temperature and composition of the matter reversible property changes is indeed possible by the varying space-charge density. The reversible variation of the paramagnetic susceptibility, χ, of Pd [29] with the charge was found consistent with band-filling and the notion of Stoner-enhanced susceptibility, suggesting that the concepts of band

magnetism in transition metals might apply to space-charge layers. The shift in the Curie temperature of (In,Mn)As is also an example of the variation of space-charge density in dilute magnetic semiconductors [30]. The application of electric field basically changes hole-mediated exchange interaction, and, therefore increases the Curie temperature.

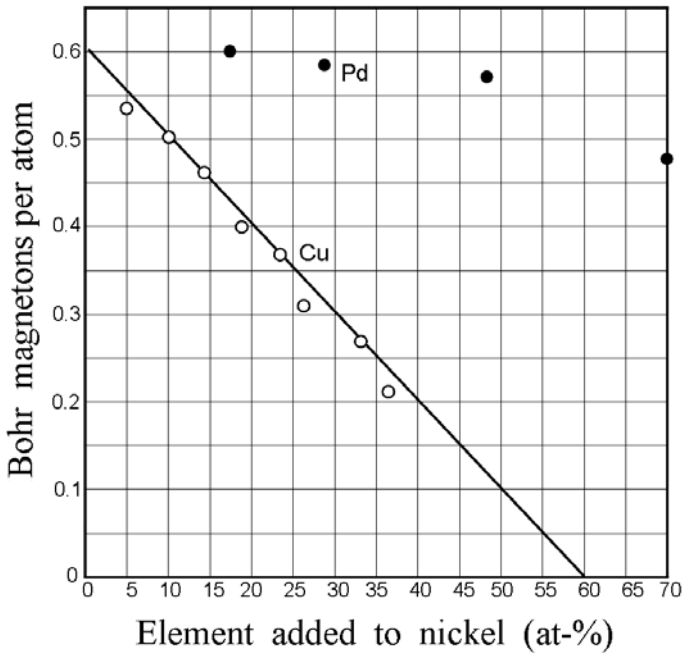

Fig. 1.3: Change in Bohr magnetons in Ni due to alloying with Cu and Pd, Bozorth R.M., Ferromagnetism, *IEEE Classic Press Reissue*, 440, 2003.

Though the recent experiments concern the change of magnetism in paramagnetic materials and semiconductors, there is not much evidence available on the change of magnetism in ferromagnetic metals using an extra charge carrier density. Experimental studies have indicated that a paramagnetic material can be made ferromagnetic by use of a surfactant on Au cluster [31]. The appearance of room temperature ferromagnetism is resulted in Au: S bonding which localises extra holes in the 5d band by the thiol ligand. The present work is further motivated by the potential controlled variation of coercivity in ferromagnetic thin film at the metal-electrolyte interface [32]. This implies that a simple reasoning might apply to the charge transfer at the surface of ferromagnets: d-band holes, responsible for ferro-

magnetism, might be filled up by excess electronic charge, and ferromagnetism thereby diminished when electrons accumulate at the surface.

1.3 Objective of the work

The objective of the present work is to observe – for the first time – reversible variations of magnetization and susceptibility of ferromagnetic transition metal alloys at room temperature. The outline of the work can be summarized as:

- Synthesizing nanoparticles and producing nanoporous materials through loose compaction.
- Characterizing samples in the dry state and in electrolyte medium. The aim of the dry measurements is to get an overview about the microstructure and the magnetic behaviour of the samples whereas wet characterization yields information about the electrochemical stability of the samples.
- Observing a change in magnetization and susceptibility of the samples while charging them within the double layer potential window as prefixed by the electrochemical characterization.

1.4 Experimental approach

The common ways for the synthesis of metallic nano-particles are mechanical alloying, chemical or electrochemical methods and thermal evaporation. Nanoparticles produced by mechanical alloying may not be a good choice due to contaminating effect of the milling medium. The problem with the chemical synthesis technique is the difficulty in removing ligands from the particle surface. By contrast, samples produced by inert gas condensation are relatively uniform in size and free from surface contamination as they are produced in an inert gas atmosphere in an ultra high vacuum chamber. Since the transition elements like Ni or Co are sensitive with respect to oxidation, a relatively less reactive element like Pd can be chosen as an alloying element. The reasons for selecting Pd-Ni or Pd-Co alloy as model systems are summarized below.

- The Curie temperature of Pd rich Ni and Co alloys lies near room temperature. Therefore, with selective variation of alloy composition it would be possible to study a single system in both ferro- and paramagnetic state at room temperature. See Fig. 1.4 for the composition dependent Curie temperature of the Ni-Pd alloys. Since electrolytes evaporate at elevated temperatures and freeze at low temperatures performing the measurement at room temperature will typically be a good choice.

- The close agreement between the vapour pressures of Pd with the alloying element (Ni or Co) enables synthesis of sample powder with desired chemical compositions and less fluctuation in chemical composition of the alloys.
- According to the binary alloy phase diagram [33, 34], Pd has unlimited solid solubility in Ni and Co, an alloy of Pd-Ni or Pd-Co can be prepared in any proportion without phase separation.

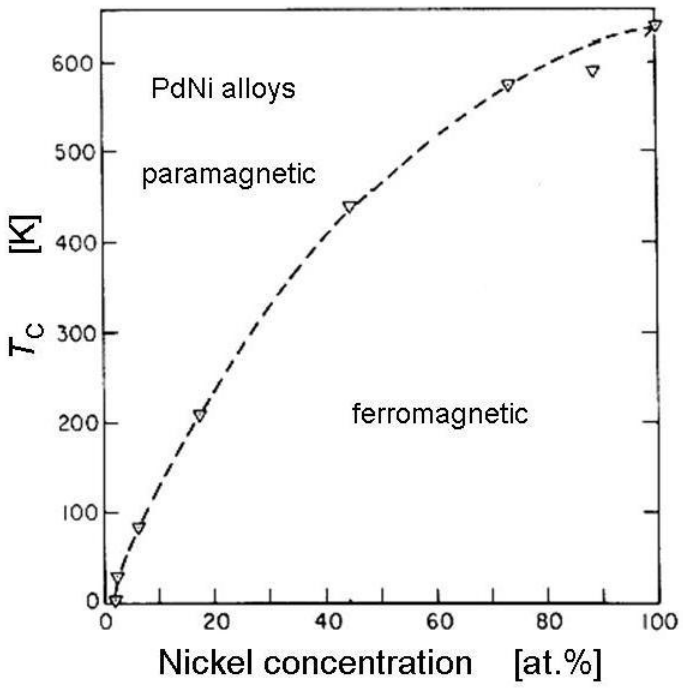

Fig. 1.4: Plot of the Curie temperature of Pd-Ni alloys as function of nickel concentration [35].

In the context of the electrochemical charging of the sample it is important to find an electrolyte which does not react with the electrode materials such as Pd-Ni and Pd-Co alloys. At the beginning of the study, a number of electrochemical experiments have been carried out to find suitable electrolyte and safe potential window susceptible for the transition metal alloys.

Recent experiments performed with the non-magnetic materials found substantial amount of strain and stress during charging of samples in electrolyte medium. Considering

the effect of stress on magnetism, *in-situ* measurements of strain has been conducted with various Pd-Ni and Pd-Co samples. The condition of the experiment was identical to the magnetic measurements for correlating the data obtained in two separate measurements.

2 Experimental procedures

2.1 Sample preparation

Nanocrystalline materials of Pd-Ni and Pd-Co alloys have been prepared by the inert gas condensation (IGC) technique. A master alloy was at first prepared by arc melting and cleaned in ethanol solution for thermal evaporation in the IGC. Figure 2.1 shows the schematic diagram of the IGC apparatus employed for the preparation of nanocrystalline powders through resistive heating of the alloy ingot.

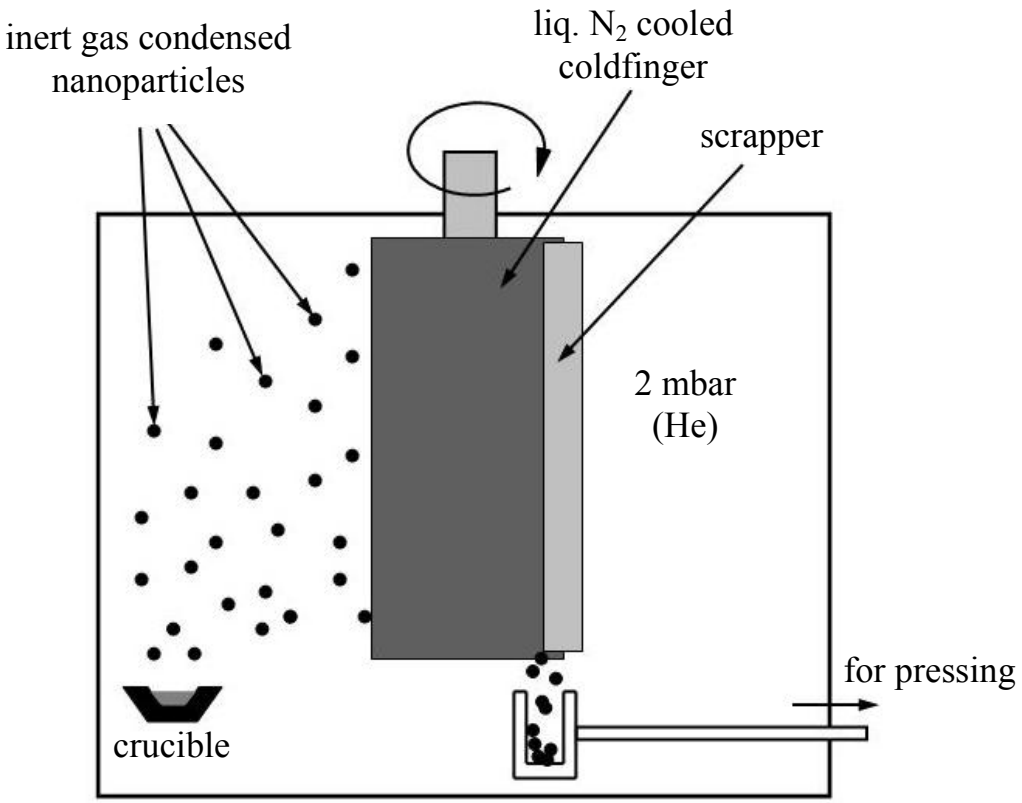

Fig. 2.1: Schematic drawing of an inert gas condensation machine for the synthesis of nanocrystalline materials.

At the beginning of the sample preparation, an alumina crucible was preheated resistively at in high vacuum for nearly half an hour to remove moisture and organic contamination (if any) entrapped into it. Heating was done at around two third of the melting point of the alloy. After cooling, the alloy ingot was loaded onto a crucible and the chamber was once again evacuated and baked at around 150^{o}C for 8-10 hours. Baking improves the vacuum level of the system as the pressure of the chamber drops to 5×10^{-8} mbar.

The sample preparation was proceeded through slow rise of the temperature of the alloy ingot. Helium gas was purged into the process chamber at a feed rate of 2000 cc/min. just before the alloy ingot starts melting. The net pressure of the chamber was maintained at 2 mbar by isolating the vacuum pumps from the synthesis unit and continuously purging helium gas inside the chamber, while the excess pressure was released through a bypass valve.

The evaporated atoms transfer their thermal energy to the inert gas and condense to the liquid-nitrogen cooled coldfinger in the form of loosely agglomerated particles. They were collected as batch of samples after scratching them out of the coldfinger. Samples were consolidated in a 3 mm diameter die at a moderate pressure of about 100 MPa to avoid complete densification of the powder, thus yielding 3×~0.5 mm (diameter×thickness) porous disks after compaction. Volume was calculated using the thickness and the diameter of the sample, assuming it as a thin cylindrical disc. After dividing volume with sample mass, the density of each disc was roughly estimated as 2.4 g/cm^3, which corresponds to about 25% of the bulk density.

Figure 2.2 shows the variation of nickel content in the Pd-Ni precursor and in the alloy particles after evaporation in the IGC. It is seen from the figure, the nickel concentration of

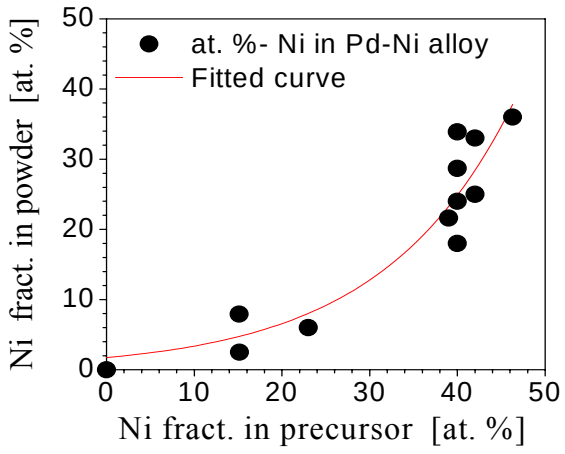

Fig. 2.2: Nickel concentration in the master alloy (precursor) used versus nickel concentration in the IGC produced nanocrystalline Pd-Ni alloy powder.

the alloy powder prepared is smaller compared to that in the precursor. Therefore, the alloy powder is initially depleted and later gets enriched with Ni. In the present case only a small fraction of the ingot was evaporated and they were collected as batch of samples in order to maintain reasonably good homogeneity of the sample composition.

2.2 Characterization

2.2.1 X-Ray diffraction

Crystal structure and microstructure of the samples were studied by X-Ray diffraction with sample pellet of the diameter 3 mm. Measurements were performed in Bragg-Brentano geometry using Cu-K_α radiation (λ = 1.54018 Å) in a Philips Analytical X'Pert diffractometer. The intensity of the diffraction beam was counted with a position sensitive detector. A mean grain size was determined by analysis of the integral breadth of the Bragg reflections, after correcting for instrumental broadening and separating size and strain induced broadening by the method of Klug and Alexander, assuming Cauchy size and Gaussian strain broadening [36]. The diffraction maxima were fitted with Pearson VII function using the Profit software to obtain the integral width of the Bragg reflection. The lattice constant was calculated from the Bragg's reflection using Nelson-Riley function, correcting for zero-angle offset, sample displacement along the scattering vector, and stacking faults of the face centred cubic crystal.

2.2.2 Composition analysis

Energy Dispersive Analysis of X-ray fluorescence (EDX) in a scanning electron microscope (SEM, LEO 1530) was used to estimate composition of alloy powder. EDX values for the Ni- or Co atomic fraction were recorded for roughly 3×10^{-4} mm^3 sized volume elements at three different arbitrary locations of the 3 mm diameter pellets. It was intentionally done to get an overview about the homogeneity of the alloy powders in each batch of the samples.

2.2.3 Electron microscopy

The microstructure was investigated with different electron microscopy. A scanning electron microscope, which was used for the EDX analysis was also employed here to verify the effect of pressure to porosity of the samples. Transmission electron microscopy (TEM) studies of alloy powders were done with a Philips FEI Tecnai F20ST field-emission gun

(FEG)-TEM operated at 200 kV. The samples were prepared by dispersing agglomerated particles in ethanol medium using ultrasonic vibration. It was later dispersed on the carbon film placed on a fine copper grid. After evaporation of ethanol, sample was inserted into the TEM.

2.2.4 Electrochemical characterization

This measurement includes cyclic voltammetry studies of the sample using it as working electrode. Several electrolytes were tested for this purpose. These are 1 M $LiClO_4$ in ethyl acetate, 1 M $LiClO_4$ in acetonitrile, 1 M $LiClO_4$ in γ-butyrolactone, 1 M KOH solution (aqueous). Emphasis was given to non-aqueous electrolytes because they are known to be less reactive with metals and can provide large electrochemical potential windows [28].

For the *ex-situ* characterization of sample, a commercially available standard glass recipient was used for the construction of a cell. A loosely compressed pellet of Pd-Ni or Pd-Co alloy was wrapped with a 0.127 mm diameter thin gold (99.99% pure) wire to be used as working electrode. Commercially available porous carbon cloth, supplied by Kynol Europa GmbH, was rolled and wrapped with the same gold wire to serve as counter electrode. The reference electrode was prepared electrochemically by depositing Cl^- ions on the Ag wire (0.5 mm diameter) at 1 V constant potential in 1 M HCl solution, using another Ag wire (a similar type) as counter cum reference electrode. The portion of the Ag wire which was exposed to electrolyte turns brownish after deposition of Cl^- ions for 1 minute. It was then removed from the acid solution and was washed under the constant flow of ultrapure de-ionised water for about 15 minutes. It was further kept in distilled water bath for more than an hour before being dried and used in the electrochemical cell.

Working, counter and reference electrode were finally connected to an electric source, such as a potentiostat (PGSTAT10, Eco Chemie) after dipping them into an electrolyte. Before using an electrolyte, it was thoroughly purged by bubbling with nitrogen, thus reducing the oxygen gas contamination. During the measurements, the applied potential was ramped from negative to positive potential and back; each measurement was repeated up to few consecutive cycles of charging. The voltammogram is obtained by plotting current against the applied voltage. A slow scan rate of 0.25 mVs^{-1} was maintained throughout the voltammetry studies to get overview of the detailed electrochemical reactions, which may not be seen at the faster scan. A few measurements were performed in a simple cell geometry using the sample as working electrode and porous carbon cloth as counter cum reference electrode. At the beginning, the two-electrode geometry was thought to be useful because constructing tiny electrochemical cell with standard reference electrode faced problem during *in-situ* magnetic measurement. An easy solution was to substituting the standard refer-

ence electrode with an electrochemically prepared Ag/AgCl reference electrode, named as pseudo-reference electrode. It was found useful for use in complex cell geometry discussed in section 2.2.6.1. At the end, the carbon electrode was calibrated with respect to standard Ag/AgCl reference electrode, using carbon cloth as working electrode and Ag/AgCl as reference electrode. A potential difference of 0.21 V was estimated and subtracted from the potential range obtained in two-electrode configuration. Never the less, measurements performed in two-electrode geometry found consistency with three-electrode configuration in terms of the net charge transferred on the sample electrode despite a small shift in the potential window.

2.2.5 Magnetic measurement

The loosely compressed pellets of the Pd-Ni or Pd-Co alloy powders were studied in magnetometers prior to immersion into electrolyte. The experimental procedures for dry characterization of the samples are described below.

2.2.5.1 Hysteresis loop

It is know that the coercivity vanishes near the Curie temperature (T_C). Therefore, coercivity obtained from the hysteresis loop can be a choice to see whether the sample retains significant coercivity at 300 K. Based on this measurement ferro or paramagnetic state of the samples can be realized at 300 K. A Quantum Design extraction magnetometer (PPMS with 9 Tesla cryomagnet) was employed to measure loops from 5 K to 340 K temperature with a maximum applied field of 6 to 9 Tesla.

Besides ZFC loops, a few hysteresis loops were measured under field cooled (FC) condition to verify possible exchange biasing [37] of the samples. For this measurement, samples were cooled down to 5 K under 9 Tesla field and then loops were measured. The presence of antiferromagnetic oxide layer causes widening [38] and shifting [38, 39] of the FC loops. Therefore, comparative analysis of loops may give an insight about the magnetic purity of the ferromagnetic samples.

2.2.5.2 AC-susceptibility

AC susceptibility was measured to verify the temperature dependent phase transition of the samples and then correlating change with the Curie or the Curie-Weiss law [13]. Measurements were performed at an AC field amplitude of 15 Oe. The frequencies were chosen as

100 Hz, 1 kHz, 5 kHz, 10 kHz. At the start of measurement, samples were cooled down to 5 K from 340 K and then susceptibility was measured during heating of the samples.

2.2.5.3 Magnetization at low field (ZFC/FC)

At a low magnetic field freezing and relaxation of the spins can be seen upon variation of temperature. Measurement of magnetization at low field may also give an idea on the ferro- to superparamagetic transition of the samples near the blocking temperature (if any).

For zero-field cooled (ZFC) experiment each sample was cooled down to 5 K temperature in the absence of magnetic field and then magnetization was measured at an applied magnetic field of 20 mT during heating of the samples. For field cooled (FC) measurement samples were again cooled down to 5 K temperature at 20 mT field followed by measurement of magnetization at the same magnetic field. For Pd-Ni samples Oxford design VSM with 12 Tesla cryomagnet was employed whereas Pd-Co samples used Quantum Design PPMS due to technical problem with the VSM.

2.2.6 *In-situ* magnetometry

This experiment was aimed at measuring the magnetization and susceptibility of the sample during electrochemical charging of the samples inside a magnetometer. The details of the experimental set up and measurement procedures are discussed below.

2.2.6.1 Expermental set up

The experimental set up was arranged in such a way that electrochemical charging of samples can be performed within a small sample space (7.7 mm diameter) of the magnetometer. A custom built electrochemical glass cell was designed for this purpose as shown in Fig. 2.3(a). The electrochemical cell consists of Pd-Ni/Co pellet as working electrode, porous carbon cloth as counter electrode and Ag/AgCl wire as reference electrode. The dimension of the working electrode is 3 mm×~0.5 mm (diameter×thickness).

Both the working and counter electrode was mounted on a thin teflon sheet by wrapping gold wire (diameter 0.127 mm) around it. The electrochemically prepared Ag/AgCl reference electrode was directly pierced through the teflon sheet to be used as reference electrode, see Fig. 2.3(a). It allows a fixed location of the reference electrode with respect to working and the counter electrode. At the end, the teflon sheet containing all the three electrodes was inserted inside a 6 mm diameter quartz glass tube filled with electrolyte.

After construction of cell, the glass tube was sealed with a tiny teflon plug to reduce the evaporation of the electrolyte. To insert the cell inside the magnetometer, the glass tube was mounted on the sample holder (carbon rod) through a drinking straw as shown in Fig. 2.3(b). The free end of the reference electrode (inside the drinking straw) was tightly fixed with the drinking straw to avoid movement of the teflon sheet as well as electrodes, see Fig. 2.3(b). Gold wire terminals of the working and counter electrode and also the reference electrode were passed through teflon seal and joined with insulated Cu wires for electrical

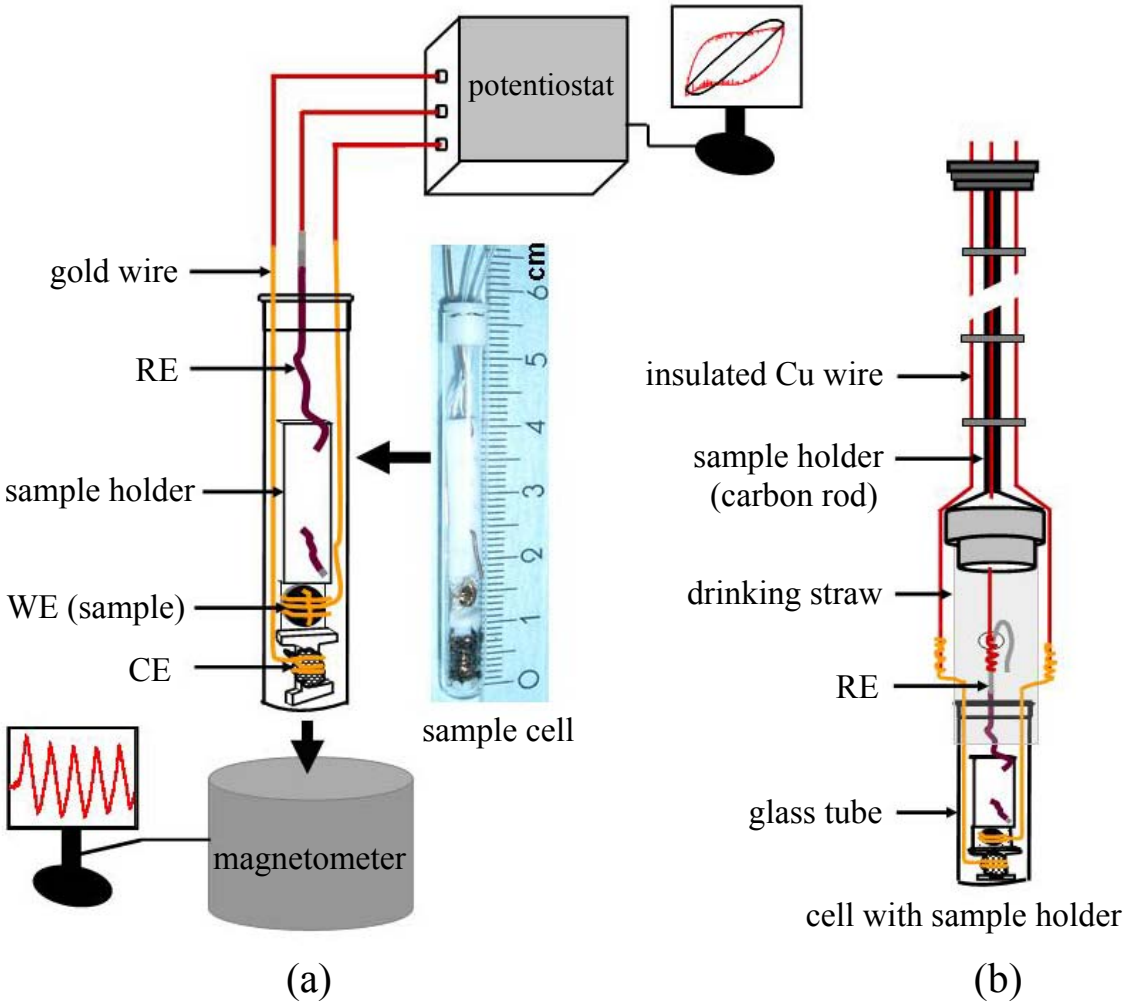

Fig. 2.3: (a) Schematic diagram of the experimental set-up for the *in-situ* magnetization and susceptibility measurements during electrochemical charging of the sample. A typical electrochemical cell is shown here using sample as working electrode (WE), porous carbon cloth as counter electrode (CE) and Ag/AgCl wire as reference electrode (RE). (b) Arrangement for mounting glass cell with sample holder.

connection with a potentiostat. For extra precaution, gold wires inside the cell were insulated by a thin teflon sleeve to avoid short circuiting of wire between working and the counter electrode. In short, the entire construction of the cell has been done in such a way that sample holder (carbon rod) and glass cell can move up and down during measurement of magnetization in extraction mode.

2.2.6.2 Expermental procedure

The *in-situ* measurements records change of magnetization and susceptibility during charging of sample inside a Quantum Design PPMS. The charging was performed via Autolab controlled potentiostat (PGSTAT 30). In order to find the correlation between magnetic data and charge value both the experiments were synchronised. Time for one full cycle of charging is [(2×potential range)/scan rate, 0.00025 Vs^{-1}]. Total time for each measurement varies depending on the number of charging cycles performed. As an example, for five consecutive cycle of charging within 1 volt potential window, the required time is around eleven hours. Based on the duration of the total charging cycle, the time for the magnetic measurements can easily be fixed. Magnetic data point was collected within a time gap of 1 to 3 minutes. The magnetometer sample space housing the cell was exposed to a constant flow of boil-off helium from the cryostat, thus preventing contamination of the cell.

The magnetic background signal was determined at various applied fields, after removing the sample from the cell, retaining the electrolyte and all other components and placing the cell in the same position as during the sample measurement.

2.2.7 *In-situ* AC-Susceptibility measurement

AC-susceptibility was measured at 300K during electrochemical charging of the sample. A small change, which may not be seen in the DC measurement, can easily be detected by AC measurement. Each measurement was carried out up to five consecutive cycles of charging within a prefixed potential window determined by the electrochemical characterization of samples.

2.2.8 *In-situ* DC-magnetization measurement

This measurement studies the change of mass magnetization during electrochemical charging of the sample. Measurements were conducted at 300K, using both the aqueous and non-aqueous electrolytes.

The experimental procedure was similar to the susceptibility measurement. Instead of AC field, a DC magnetic field was used for the measurement of magnetization. For a defined magnetic state the sample was first saturated at 8 T field before reducing H_a to the measurement field. A constant magnetic field, H_a, was applied during several successive CV's, using roughly one measurement per minute in extraction mode. These experiments were carried out with samples of the following composition: $Pd_{1-x}Ni_x$ [x = 26, 33, 40, 65] and $Pd_{1-x}Co_x$ [x = 6, 10, 22, 28, 32]; the applied field range was 3 mT to 8 T.

A few set of experiments was performed with $Pd_{67}Ni_{33}$ alloy sample in 1 M KOH solution in order to compare changes of the magnetization obtained in non-aqueous electrolyte.

2.2.9 *In-situ* strain measurement

This experiment measures strain in both the Pd-Ni and Pd-Co alloys during electrochemical charging of the samples. A custom built miniaturised glass cell housed in the working place of a commercial dilatometer (Linseis) was used for this purpose, see Fig. 2.4. The charging procedure was similar to the *in-situ* magnetic measurement.

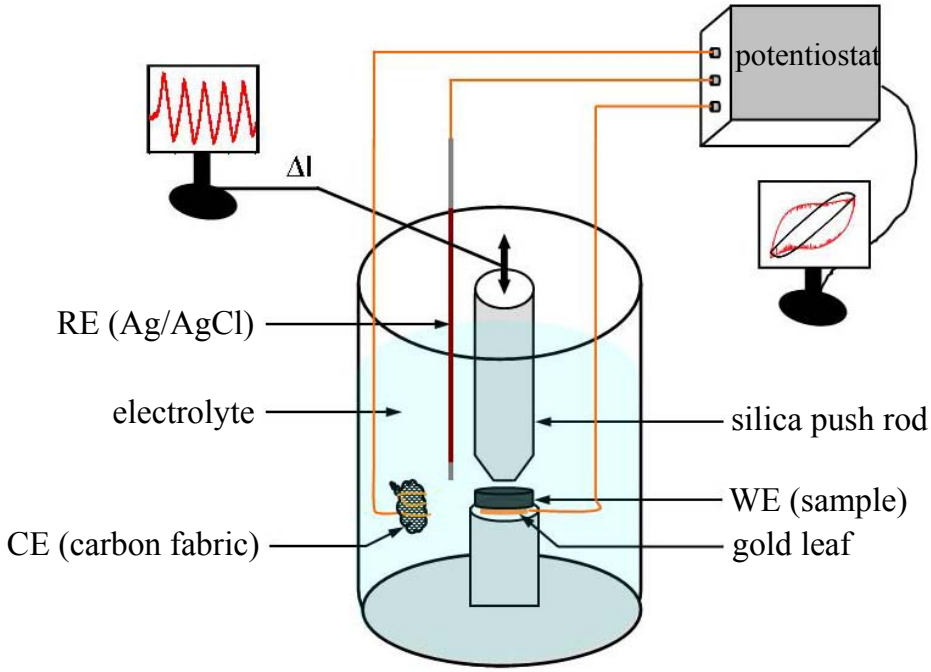

Fig. 2.4: Schematic diagram of the experimental set-up designed for the *in-situ* measurements of strain in dilatometer; WE = working electrode, CE = counter electrode, RE = reference electrode.

The glass cell contains sample as working electrode, porous carbon cloth as counter electrode and Ag/AgCl wire as reference electrode. They were connected to a potentiostat (Autolab PGSTAT 100) for charging of the samples in 1 M $LiClO_4$ in ethyl acetate. Sample was placed on a thin gold leaf for better electrical contact with the gold wire. For more information see Refs. [16, 24]. Potential was cycled at the scanning rate of 0.25 mVs^{-1}, which is same as that of the *in-situ* magnetic measurements. At the beginning of the measurement sample position was initialized to zero position.

Both the Pd-Ni and Pd-Co alloy system were studied with different Ni and Co fraction. During charging, silica push rod, which hold the sample pellet with the base support, moves up and down in accordance with the volumetric expansion/contraction of the porous sample and measures the length change. This quantity was later divided with the length of the sample (here thickness) to get strain in both the alloy systems. Electrolyte was purged with N_2 gas bubble prior to use and a few measurements were performed with continuous flow of argon gas during *in-situ* charging of the samples in the dilatometer. Temperature of the electrolyte was fixed to 287 K by passing cold water through a metal case housing the electrochemical cell.

3 Experimental results

3.1 X-Ray diffraction

The intensity of the X-ray diffracted beam plotted against scattering angle, 2θ for the Pd-Ni alloy samples is shown in Fig. 3.1. (a).

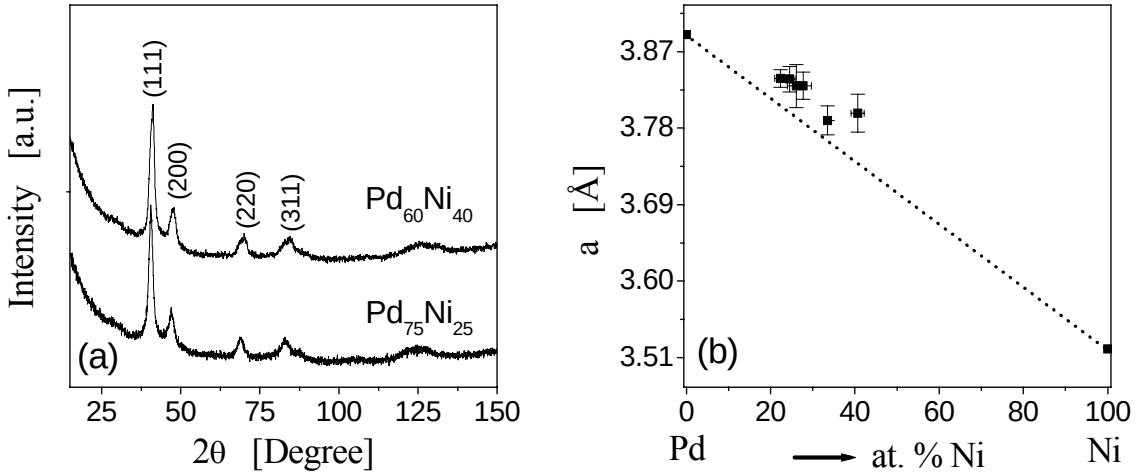

Fig. 3.1: (a) X-Ray diffraction intensity versus scattering angle 2θ for nanocrystalline Pd-Ni alloys. (b) Lattice constant of nanocrystalline alloy particles with the variation of alloy composition. Lattice constant of the bulk Pd and Ni are included in the figure for comparison.

The Miller indices of the peaks are shown in Fig. 3.1(a) and in Fig. 3.2(a) for indexed for Pd-Ni and Pd-Co alloys respectively. The superposition of nickel and cobalt peaks with palladium suggests that a single phase exists in the binary alloys due to complete solid solubility of palladium with nickel [33] and cobalt [34] atoms. The X-Ray diffraction patterns, however, do not show any signature of oxide [40, 41, 42] phase in both the alloy particles

as lattice constant measured with various Pd-Ni alloys decreases systematically with the variation of the alloy composition as shown in Fig. 3.1(b). The area weighted crystallite size $\langle D \rangle_A$ for the Pd-Ni and Pd-Co alloys are in the range of 6±2 nm. This value was further crosschecked by TEM micrograph in section 3.3.3.

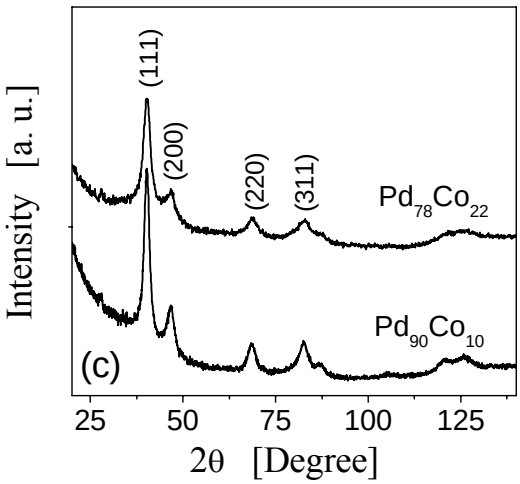

Fig. 3.2: (a) X-ray diffraction intensity versus scattering angle 2θ for nanocrystalline Pd-Co alloys.

3.2 Composition analysis

The result of energy dispersive analysis of X-ray (EDX) fluorescence indicates a maximum variance of 2 at. % in the composition in each batch of the samples. This measurement also found, individually, a small traces (<1 at.-%) of elemental C, Al in alloy powder along with Pd, Ni or Co. A possible source of Al could be the sample holder on which porous sample was mounted for EDAX analysis. As carbon film is usually used to fix sample with the holder, so its presence could also be detected in the EDX analysis.

3.3 Electron microscopy

3.3.1 Scanning electron microscopy (SEM)

Figure 3.3 shows a scanning electron microscopy image of the $Pd_{72}Co_{28}$ alloy pellet. The loose consolidation of the powders leaves the pellet with a non-uniform pore distribution

throughout the sample. A similar bicontinuous structure, formed by the interconnected network of nanometer-sized crystallites and the pore space, can be seen after loose compaction of powder in the grain size of roughly 6 nm [16].

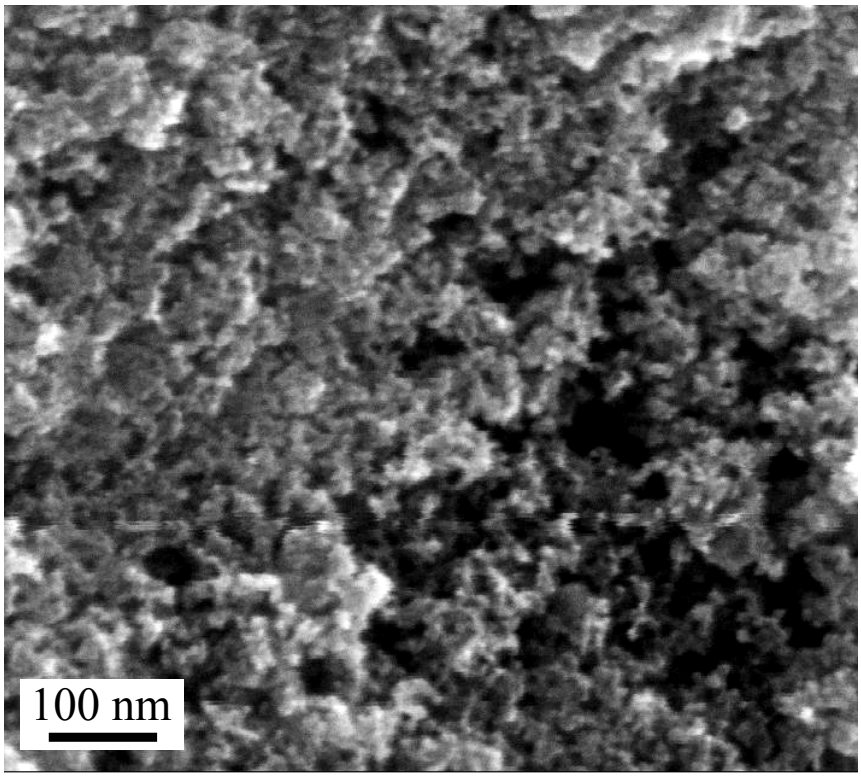

Fig. 3.3: Scanning electron micrograph of a lightly compressed $Pd_{72}Co_{28}$ alloy pellet showing the porous nature of the sample.

3.3.2 Transmission electron microscopy (TEM)

The powder produced by inert gas condensation method resembles to nano-clusters as shown in TEM micrograph of the $Pd_{60}Ni_{40}$ alloy sample in Fig. 3.4. The agglomerating nature of particles is a reason for the particles remain interconnected with each others. There-

fore, magnetic properties of the samples are expected to be different than the fine particles remain dispersed in the nanometer scale.

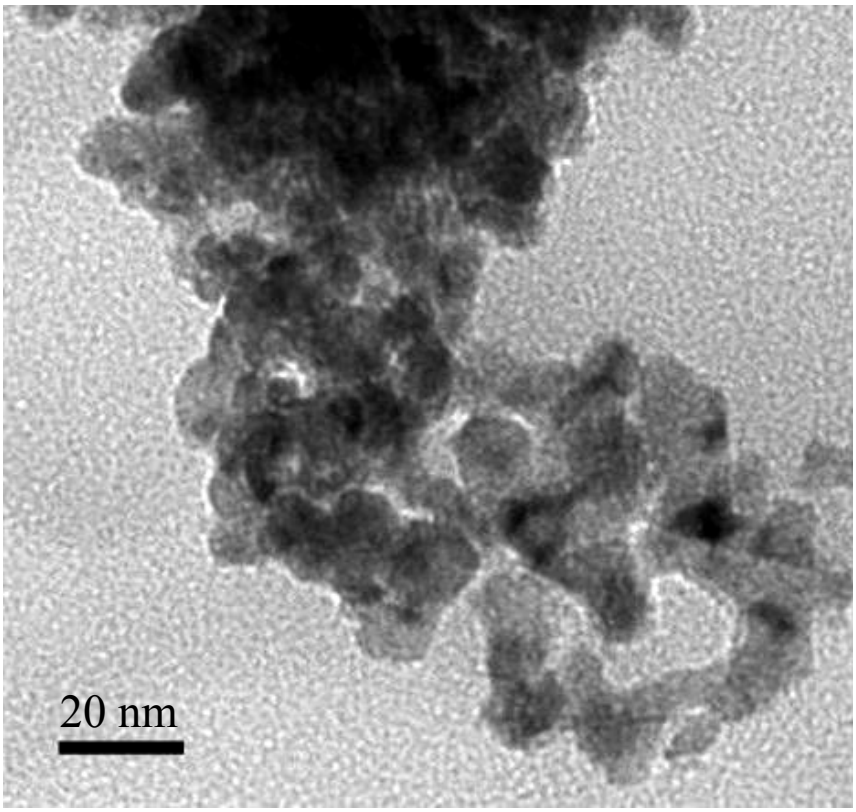

Fig. 3.4: TEM image of the loose $Pd_{60}Ni_{40}$ alloy particles showing the agglomerating nature of the nanoparticles synthesized by the inert gas condensation method.

3.3.3. High resolution TEM

The high resolution TEM image of the $Pd_{82}Co_{18}$ alloy particles reveals that the particles are crystalline and that the size of the crystallites may vary within 6-7 nm as shown in Fig. 3.5. Well defined lattice fringes can be seen extending all the way from surface to interior of the individual particles. If oxidation has to be admitted, an amorphous oxide layer [43] would be expected at the surface of the particles. The bright contrast as seen along the surface of

the particles is the Fresnel fringes. They may not be related to the oxide layer. The chain like appearances of the particles as shown in Fig. 3.5 could be attributed to the metallic grain boundaries form at the surfaces of the particles.

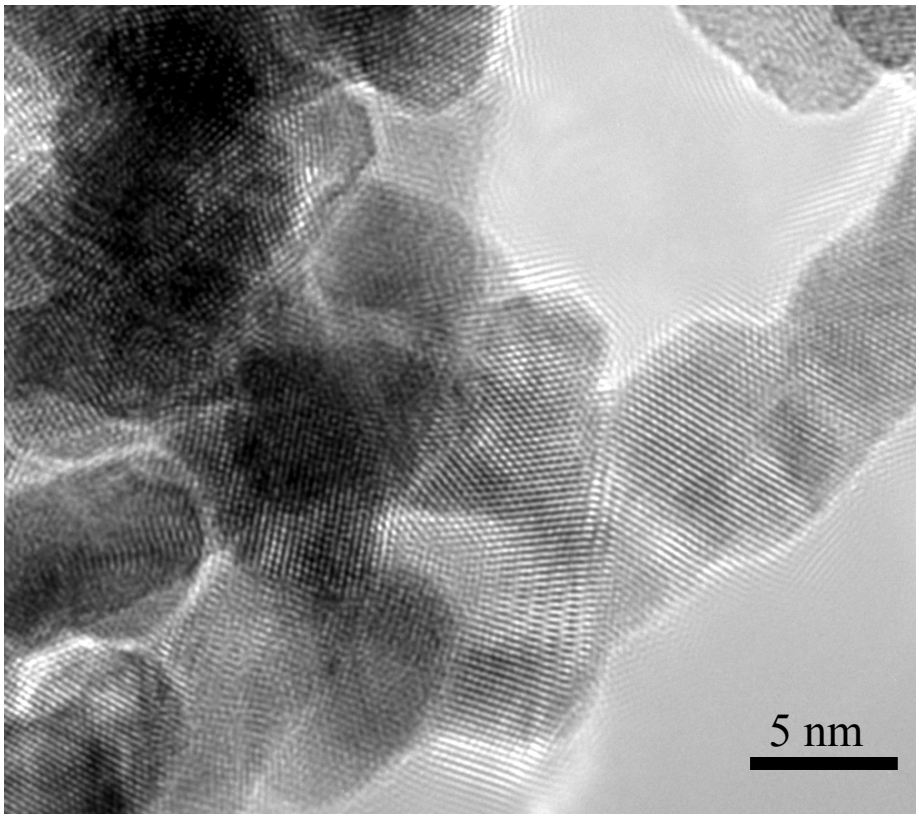

Fig. 3.5: High resolution TEM image of the IGC prepared $Pd_{82}Co_{18}$ alloy particles showing lattice fringes extending from surface to interior of the individual crystallites.

The concluding remarks on the microstructure studies of the sample in electron microscopy can be summarised as following:

- The samples produced by the IGC method consist of interconnected nanocrystals with a size range of 6-7 nm.
- There is no experimental evidence about the presence of an oxide layer at the surface or interior of the alloy particles.

3.4 Electrochemical measurements

The following section discusses the electrochemical processes through comparative studies of voltammograms in 1 M KOH and in 1 M $LiClO_4$ in ethyl acetate. Though measurements were initially started with a number of electrolytes, a part of them was later rejected due to high evaporation rate of the acetonitrile solution and slow charge transfer kinetics in gamma-butyrolactone. Finally, an aqueous electrolyte, KOH, and a non-aqueous solvent, ethyl acetate, has been selected. From the chemical formula ($CH_3COOCH_2CH_3$) of ethyl acetate, it is clear that it is an organic ester of acetic acid and ethyl alcohol.

3.4.1 Characterization in aqueous electrolyte

Figure 3.6 shows the cyclic voltammogram performed with a $Pd_{67}Ni_{33}$ working electrode in 1 M KOH solution. The charge, ΔQ transferred to the sample, obtained from the current integration is displayed in the right ordinate. The cyclic voltammogram exhibits important features of the transition metal alloys in aqueous electrolytes, namely OH^- adsorption (causing oxidation) /desorption [44] peaks at positive potentials and hydrogen [45, 46] adsorption and hydrogen gas evolution at negative potentials.

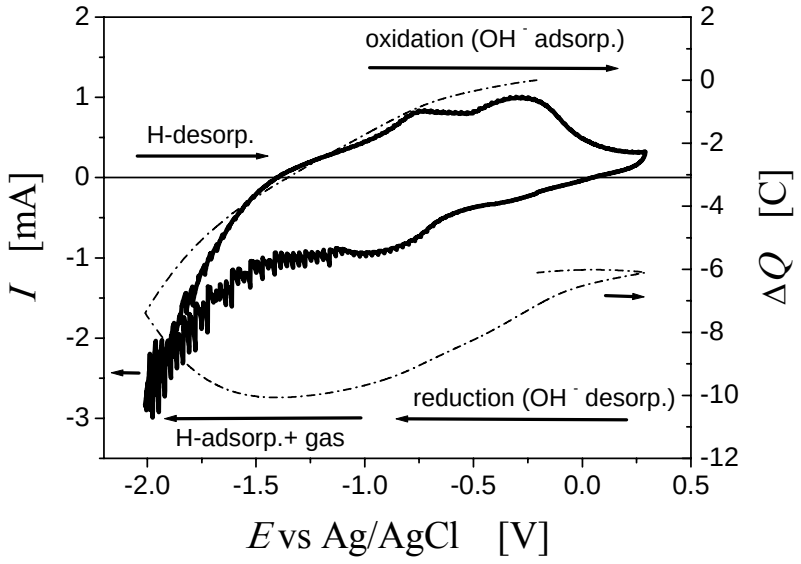

Fig. 3.6: Cyclic voltammogram measured with $Pd_{67}Ni_{33}$ electrode in 1 M KOH solution, showing the variation of current, *I*, and of net transferred charge, ΔQ, against applied potential, *E*. Hydrogen gas evolutions can be seen at negative-*E*. ΔE measured in two-electrode geometry has been normalized to Ag/AgCl reference electrode potential.

It is also seen from the figure that the electrode current, *I* starts to fluctuate at more negative-*E* (below −1.1 V) where gas bubbles were observed due to decomposition of water molecules present in the aqueous medium. The potential window between the reaction signals, the large current of the hydrogen evolution at negative potentials and the peaks at more positive potentials, is quite small, indicating a small stability window for the combination of $Pd_{67}Ni_{33}$ and the electrolyte.

3.4.2 Characterization in non-aqueous electrolyte

The utility of the selection of non-aqueous electrolyte is to avoid the water molecule present in the aqueous medium. The main reason for the selection of ethyl acetate is it does not readily react with nickel and its alloy [47]. The solubility for $LiClO_4$ salt in ethyl acetate is maximum 95.12 g per 100 g solvent and the dielectric constant is 6. The dielectric behaviour enhances capacitive charge layers at the alloy-electrolyte interfaces. [48].

Figure 3.7 shows a typical cyclic voltammogram of $Pd_{60}Ni_{40}$ alloy electrode in 1 M $LiClO_4$ in ethyl acetate measured in the potential interval, −1.0 to 1.5 V. The cyclic voltammogram exhibits nearly a constant current region (capacitive) from −0.4 to 1 V. Above 1 V positive-*E* the anodic current increases significantly, most likely due to a reaction of the solvent, e.g., $2H_3C–COOC_2H_5 \rightarrow H_3C–C(–O–C_2H_5)–O–CH_2–C(OH)–O–C_2H_5 + 2e^-$.

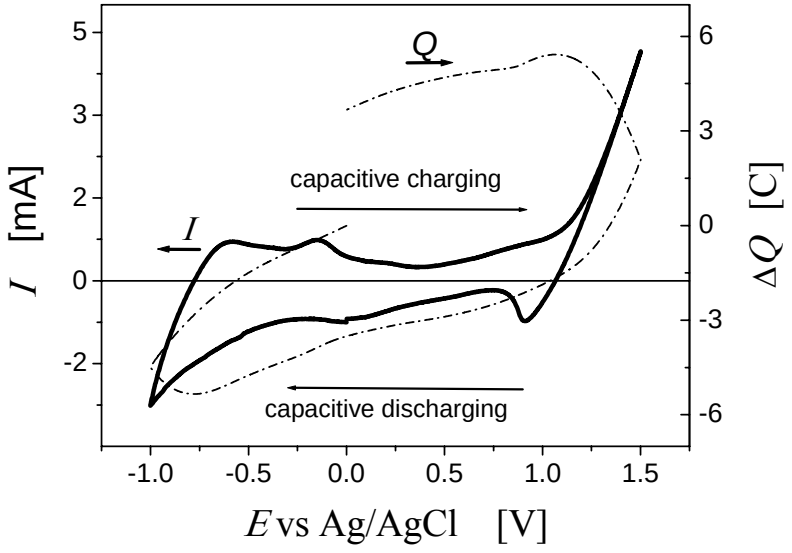

Fig. 3.7: Variation of the current, *I*, and of the net transferred charge, Δ*Q* (dotted line), on $Pd_{60}Ni_{40}$ electrode showing a nearly constant current window (capacitive) up to 1.5 V in 1 M ethyl acetate solution.

Figures 3.6 and 3.7 demonstrate that net charge, ΔQ transferred versus E curves are not closed, caused by the irreversible charge transfer reactios, hydrogen evolution and electrolyte decomposition respectively. Hence, for further analysis, the applied potential was restricted to a small ΔE where surface specific adsorption could be minimized.

Figure 3.8 shows the cyclic voltammograms of $Pd_{65}Ni_{35}$ and $Pd_{72}Co_{28}$ in 1 M $LiClO_4$ in ethyl acetate solution. It exhibits absence of reaction peaks and continuous charging and discharging of the samples within the selected range of the applied potential, E; suggesting that capacitive processes are dominating in these regions. The net charge on $Pd_{65}Ni_{35}$ and $Pd_{72}Co_{28}$ electrode obtained from peak-to-peak amplitude of ΔQ is 0.14C and 0.45C, respectively.

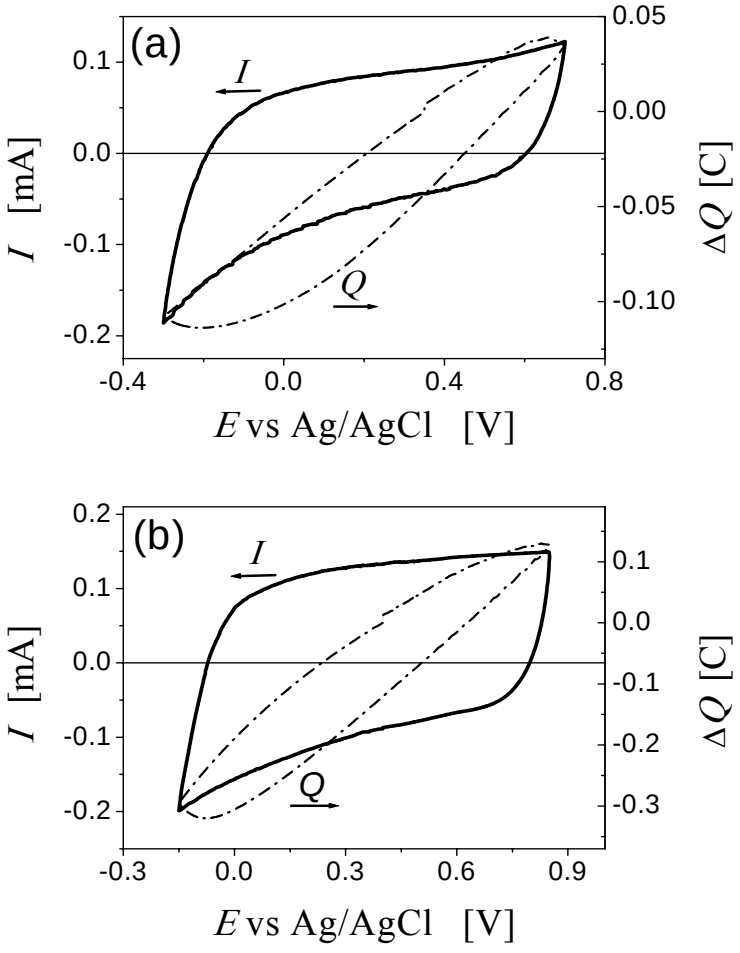

Fig. 3.8: The cyclic variation of current, I in (a) $Pd_{65}Ni_{35}$ and (b) $Pd_{72}Co_{28}$ alloy electrodes indicating the absence of a reaction peak within the selected range of the applied voltage, E. The reversible variation of net charge, ΔQ transferred on both the alloy electrode indicating negligible current loss compared to the previous measurements at larger ΔE.

3.5 Magnetometry

3.5.1 Magnetization isotherm

Figure 3.9(a) shows the isotherm of the mass magnetization measured with various Pd-Ni alloys at 300 K. The magnetization curve characterises the samples as a soft ferromagnet with small amount of coercivity can be seen at the inset of Fig. 3.9(a).

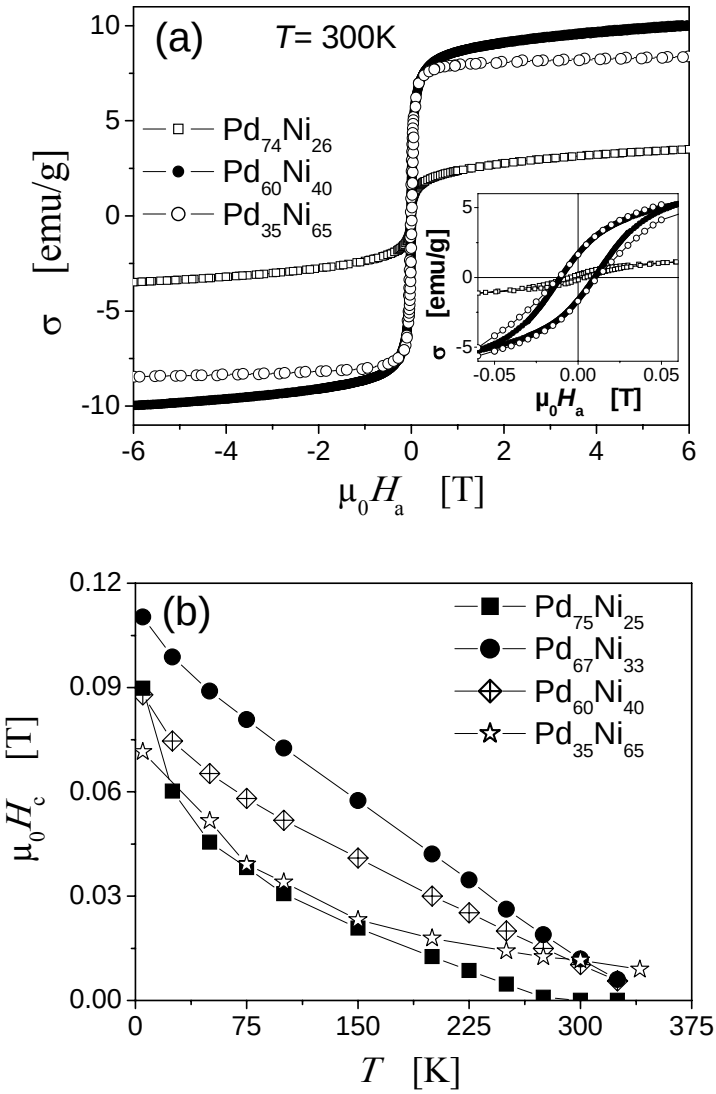

Fig. 3.9: (a) Magnetization isotherm measured at $T = 300$ K showing variation of mass magnetization, σ with the applied magnetic field, H_a. (b) Coercivity, H_C obtained from the hysteresis loops showing variation of H_C with T for the various Pd-Ni alloys.

It is also shown that samples are reasonably saturated at 6 T applied magnetic field. The saturation magnetization of $Pd_{60}Ni_{40}$ is around 10 emu/g, which is higher than that of $Pd_{35}Ni_{65}$ and $Pd_{74}Ni_{26}$ samples. Similar effect can be seen in Fe-Co alloys where saturation magnetization increases with the increase of cobalt concentration up to about 27 wt. %, but falls down sharply with further increase of the cobalt concentration [13]. Again, the saturation magnetization measured separately in the arc melted $Pd_{67}Ni_{33}$ and $Pd_{58}Ni_{42}$ alloys is 20 emu/g and 28 emu/g respectively, which is obviously higher than the values obtained

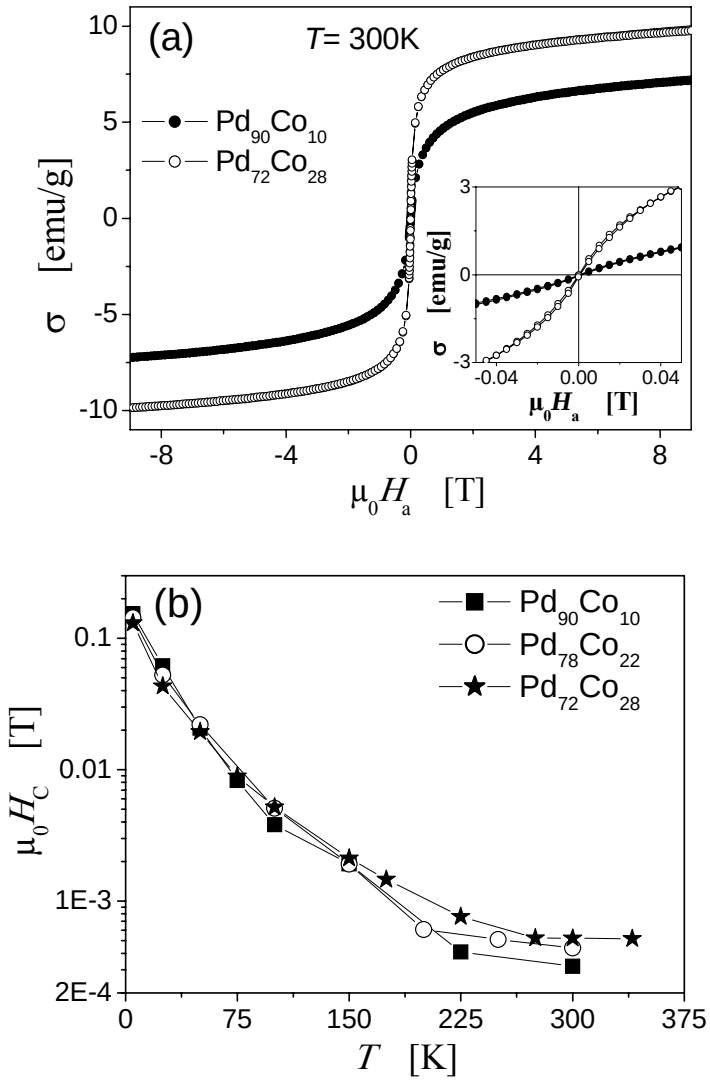

Fig. 3.10: (a) Isotherm of the mass magnetization σ versus applied magnetic field, H_a for various Pd-Co alloys at T = 300 K and (b) coercivities H_C (log scale) obtained from the hysteresis loop showing variation of H_C as a function of T.

in the nanocrystalline samples. A possible reason could be the surface oxidation and the effect would be consistent with the reversible oxidation/reduction behaviour of Pd-Ni in KOH solution. It is also seen that coercivity, H_C, decays with the increase of temperature in Pd-Ni alloys and at 300 K, H_C tends to converge at a constant value for all the sample compositions, still $Pd_{35}Ni_{65}$ alloy exhibits slightly higher coercivity value than that of the $Pd_{1-x}Ni_x$ [x = 33, 40, 26] alloys as shown in Fig. 3.9(b).

Figure 3.10(a) shows the magnetization curves of the Pd-Co alloys. At any given temperature the coercivity values [fig. 3.10(b)] of the alloy compositions are nearly the same. It is also shown that the coercivity of the alloy samples sharply falls with temperature compared to Pd-Ni alloys. Figure 3.11 shows that hysteresis loops measured with $Pd_{68}Co_{32}$ alloy retain same coercivity in both the field (FC) and zero-field (ZFC) cooling of the sample. Shifting or broadening of the FC loop could not be seen on cooling the samples from the maximum accessible temperature (340 K).

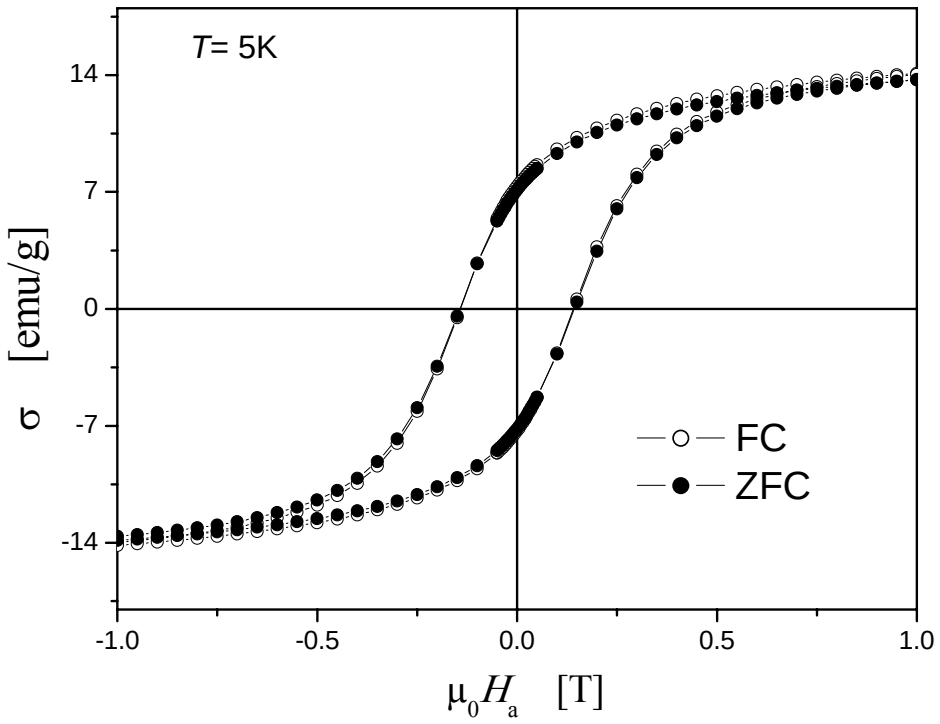

Fig. 3.11: Hysteresis loops measured at 9 T under the field (FC) and zero-field (ZFC) condition of cooling, showing the absence of exchange biasing in $Pd_{68}Co_{32}$ alloy at measurement temperature, T = 5 K.

3.5.2 AC-susceptibility

The real part of the AC susceptibility, χ', measured with various Pd-Ni and Pd-Co alloys is shown in an exemplary plot for the $Pd_{90}Co_{10}$ alloy in Fig. 3.12(a). The susceptibility increases with temperature, exhibiting a maximum near 175 K and then falls sharply with further increase of temperature. The reciprocal susceptibility (1/χ') when plotted against T exhibits a curved shape as shown in Fig. 3.12(b). The non-linear variation of the plot [Fig. 3.12(b)] could not be correlated with the Curie or Curie-Weiss law [13]. So, ferro- to para- or superpara-magnetic transition of the samples could be excluded here.

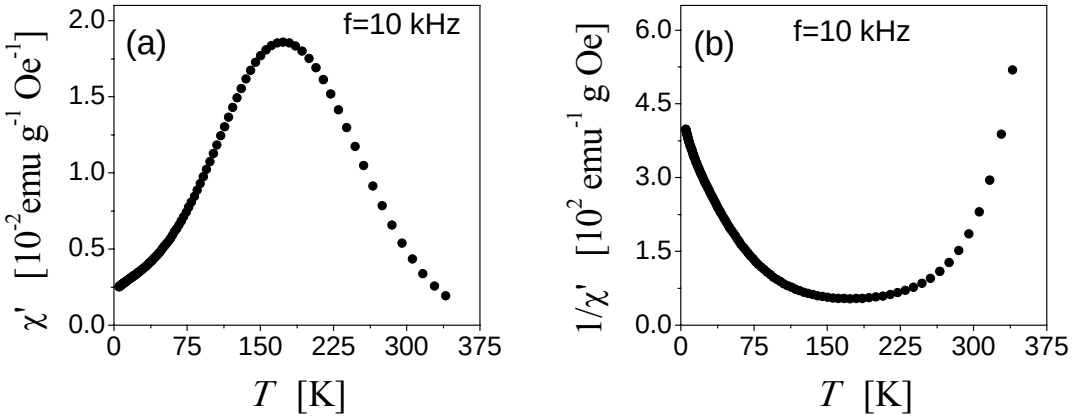

Fig. 3.12: (a) Mass susceptibility χ' plotted against temperature, T in $Pd_{90}Co_{10}$ alloy showing a broad maxima at the intermediate temperature range. (b) Reciprocal susceptibility (1/χ') plotted against T exhibits curvature shape.

3.5.3 Magnetization versus temperature

Magnetization versus temperature measured with Pd-Ni alloy under field (FC) and zero field (ZFC) condition of cooling has been shown in Fig. 3.13(a). $Pd_{75}Ni_{25}$ alloy exhibits a small rise of the magnetization (σ) curve during ZFC measurement of the sample but the FC curve steadily decays with rise of temperature until they merge at higher temperatures. In contrast to that ZFC curve of the $Pd_{90}Co_{10}$ alloy displays broad maxima at around 145 K, before it gets superimposed with FC curve in Fig. 3.13(b).

At the start of the *ZFC* measurement, magnetic moment is randomly frozen along the particles' easy axes. As the temperature increases, magnetization also increases because thermal energy slowly frees the spins and aligns them along the field direction. The cusp, which can be seen near 145 K of the ZFC curve [Fig. 3.13(b)] signifies a temperature at

which coercive field (2.5 mT) is nearly comparable to the applied magnetic field (20 mT) [49]. A steep rise at the ZFC curve of Fig. 3.13(b) may be attributed to the temperature dependent coercivity change of the sample which falls sharper in $Pd_{90}Co_{10}$ alloy than that in the $Pd_{75}Ni_{25}$ alloy. See Fig. 3.9(b) and 3.10(b) for the relative change of coercivity with temperature in both the alloys.

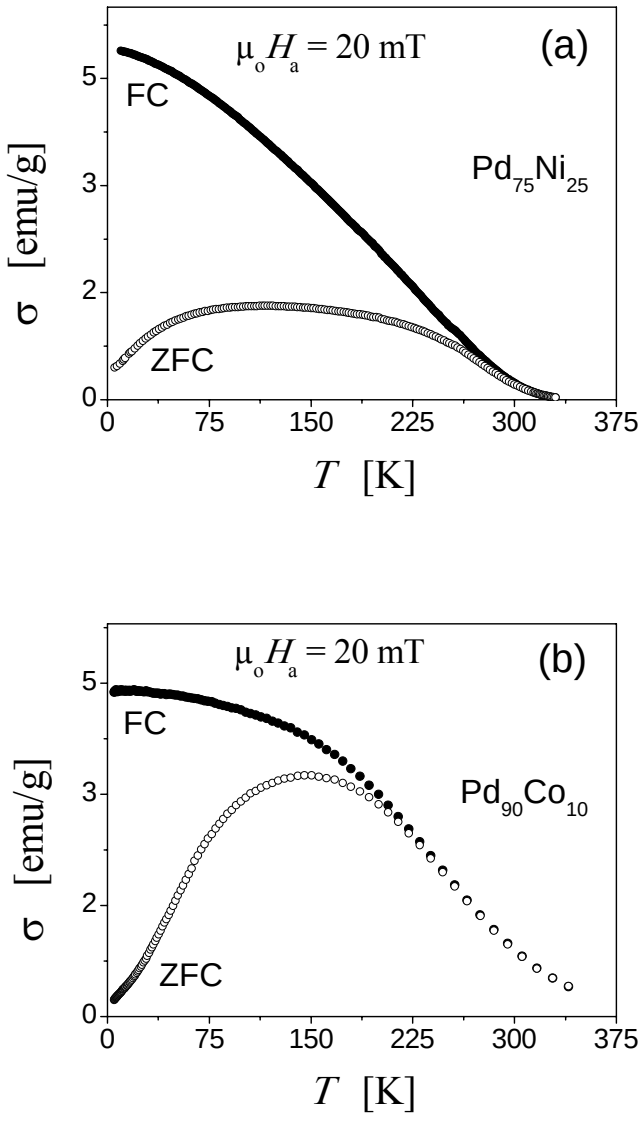

Fig. 3.13: Mass magnetization, σ plotted against measuring temperature, T showing the variation σ at H_a = 20 mT field in both the (a) $Pd_{75}Ni_{25}$ (b) $Pd_{90}Co_{10}$ alloys after cooling sample in the absence (ZFC) or presence (FC) of the measuring field.

3.6 *In-situ* magnetometry

The following section discusses the results of the AC-susceptibility and DC magnetization measured with Pd-Ni and Pd-Co alloys *in-situ* during cyclic variation of the applied potential.

3.6.1 *In-situ* AC-susceptibility measurement

Figure 3.14 shows the result of the *in-situ* measurements of susceptibility, χ', in 1 M $LiClO_4$ in ethyl acetate solution. By comparing the susceptibility data (bottom) of Fig. 3.14(a) and Fig. 3.14(c) with the potential (E) transient (top) it is seen that χ' varies reversibly in phase with the applied potential.

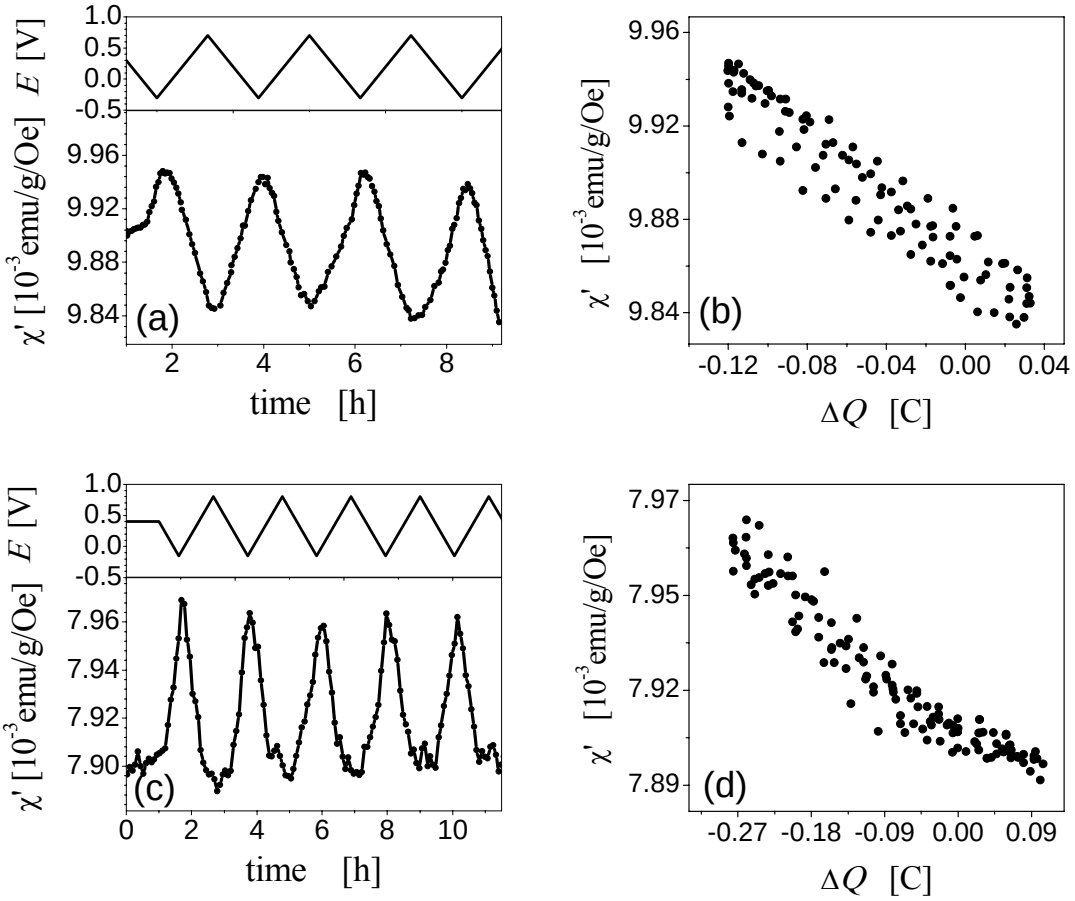

Fig. 3.14: Variation of the susceptibility, χ', and applied voltage, E with time at T = 300 K at AC field amplitude of 15 Oe in (a) $Pd_{65}Ni_{35}$ and (c) $Pd_{72}Co_{28}$. A linear correlation between χ' and excess charge, ΔQ, is found for $Pd_{65}Ni_{35}$ (b) and $Pd_{72}Co_{28}$ (d) alloys.

With respect to peak-to-peak amplitude of the χ', a maximum relative change of about 1% was found in $Pd_{35}Ni_{65}$ and $Pd_{72}Co_{28}$ alloys. Susceptibility plotted against charge, ΔQ, reveals a linear correlation in both the alloy systems irrespective of the nickel or cobalt content of the alloys as shown in a typical plot of the Pd-Ni [Fig. 3.14(b)] and Pd-Co alloy [Fig. 3.14(b)]. From the best linear fitting of the susceptibility-charge plot, $\delta\chi'/\delta Q$ was obtained.

Figure 3.15 exhibits the summary of the AC measurements performed with various Pd-Ni and Pd-Co alloys. It is seen from Fig. 3.15(a) that $\delta\chi'/\delta Q$ can have positive and negative sign in Pd-Ni alloys whereas same measurements yield $\delta\chi'/\delta Q < 0$ in all the Pd-Co alloys as shown in Fig. 3.15(b). However, the overall change of the magnitude of $\delta\chi'/\delta Q$ in Pd-Ni is nearly the same compared to that in Pd-Co alloys. The error bar shown in Fig. 3.15 indicates the standard deviation of the linear fit between χ' and ΔQ [Fig. 3.14(b, d)].

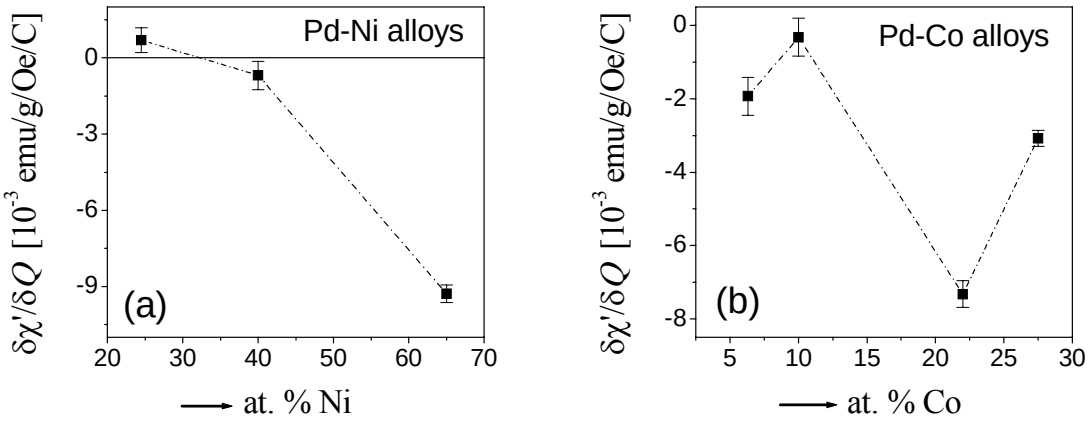

Fig. 3.15: The composition dependent variation of the susceptibility-charge coefficient, $\delta\chi'/\delta Q$ showing positive and negative values in (a) Pd-Ni alloy whereas only negative values in (b) Pd-Co alloys.

The important points highlighted from the *in-situ* measurements of susceptibility are as follows:

- A linear variation of the susceptibility with the excess charge, ΔQ.
- The maximum relative change of the susceptibility is roughly 1% in both alloy systems.
- Positive and negative sign of $\delta\chi'/\delta Q$ occur in Pd-Ni alloys whereas only negative sign of $\delta\chi'/\delta Q$ is observed in Pd-Co alloys.

3.6.2 *In-situ* DC-magnetization measurement

The DC magnetization measurements are discussed separately based on the electrochemical behaviour of the samples in non-aqueous and aqueous electrolytes.

3.6.2.1 Measurements in non-aqueous electrolyte

Figure 3.16 shows results of *in-situ* measurements of the magnetization, σ, in 1 M $LiClO_4$ in ethyl acetate solution. By comparing the magnetization data (bottom part) of [Fig. 3.16(a)] and [Fig. 3.16(c)] with the potential (E) transient (top) it is seen that the magnetization varies reversibly and reproducibly with the electrode potential, E.

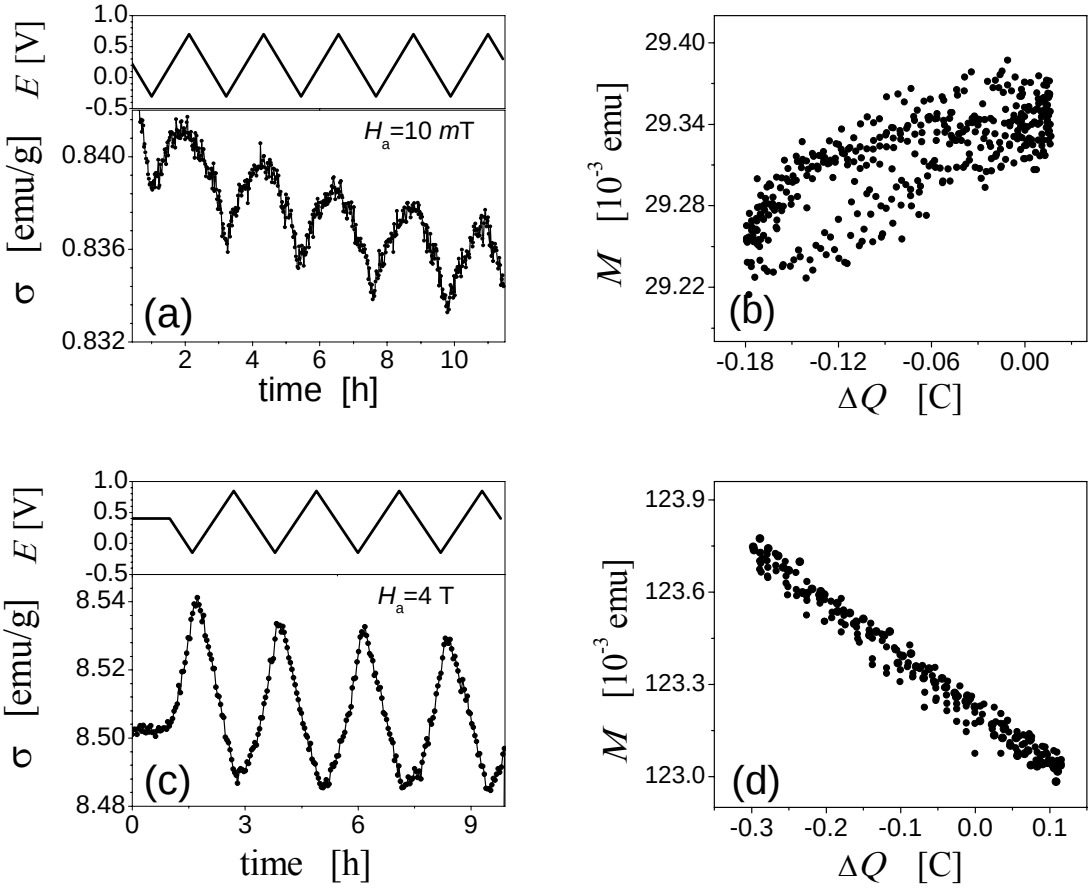

Fig. 3.16: Variation of the magnetization σ and the applied voltage, E, with time at T = 300 K in an applied magnetic field of (a) 10 mT for $Pd_{74}Ni_{26}$ and (c) 4 T for $Pd_{72}Co_{28}$, resulting linear correlation between σ and charge variation ΔQ in (b) $Pd_{74}Ni_{26}$ and (d) $Pd_{72}Co_{28}$ alloys.

A comparison of the $Pd_{74}Ni_{26}$ data in Fig. 3.16(a) to that of $Pd_{72}Co_{28}$ in Fig. 3.16(c) exhibits a 180° phase shift for the latter. Plots of the magnetization, M, versus the net charge, ΔQ, transferred to the sample [Figs. 3.16 (b, d)] exhibit an essentially linear relation. Qualitatively similar data were obtained for all compositions and applied field values studied [50, 51].

As a convenience measure for the response of the magnetization to (surface) charging, this section introduces a quantity 'magnetization-charge coefficient', $\delta M/\delta Q$, obtained from the slope of the straight lines of best fit in the graphs of Figs. 3.16 (b, d). This is an effort to couple all the variables in a single plot [Fig. 3.17], summarizing the net change of M to the net charge of ΔQ in the Pd-Ni and Pd-Co alloys as a function of sample compositions and the applied magnetic field, H_a. It is apparent that though the general magnitude of the magnetization- charge coefficient is similar for both the alloys, the dependency on H_a and the composition is significantly different for Pd-Ni [Fig. 3.17(a)] and Pd-Co alloys [Fig. 3.17(a)]. The error bar shown in Fig. 3.17 is attributed to the standard deviation of the linear fit to the Fig. 3.16(b, d), correlating ΔQ to the change of M.

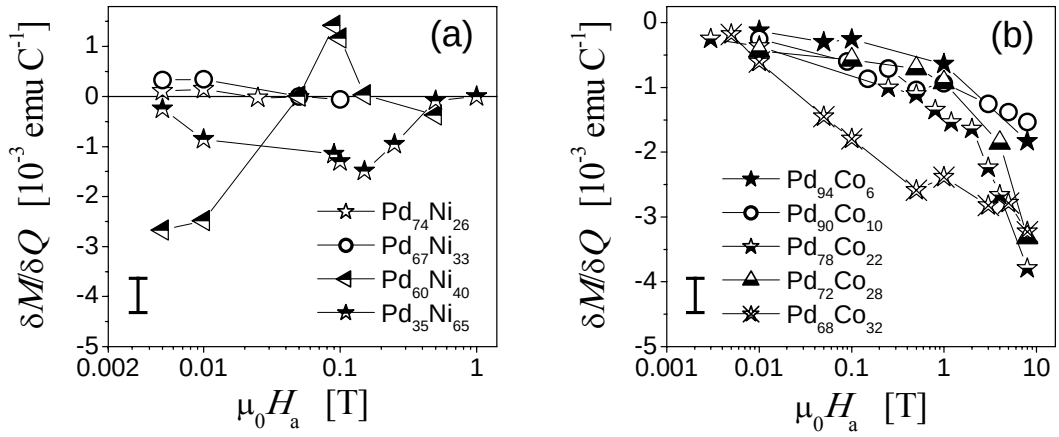

Fig. 3.17: Variation of the magnetization-charge coefficient, $\delta M/\delta Q$, with applied magnetic field, H_a, for various (a) Pd-Ni and (b) Pd-Co alloys.

The important messages that one can draw on the magnetization-charge response in the Pd-Ni and Pd-Co alloys are as follows:

- $\delta M/\delta Q$ can be negative or positive in the Pd-Ni alloys, depending on the variation of the magnetic field and the sample composition, whereas a negative value is found for the Pd-Co alloys at all the magnetic field and the sample compositions studied.
- $\delta M/\delta Q$ tends to be zero in Pd-Ni alloys near 1 T field whereas an increasing trend can be seen in Pd-Co alloys up to 8 T field.

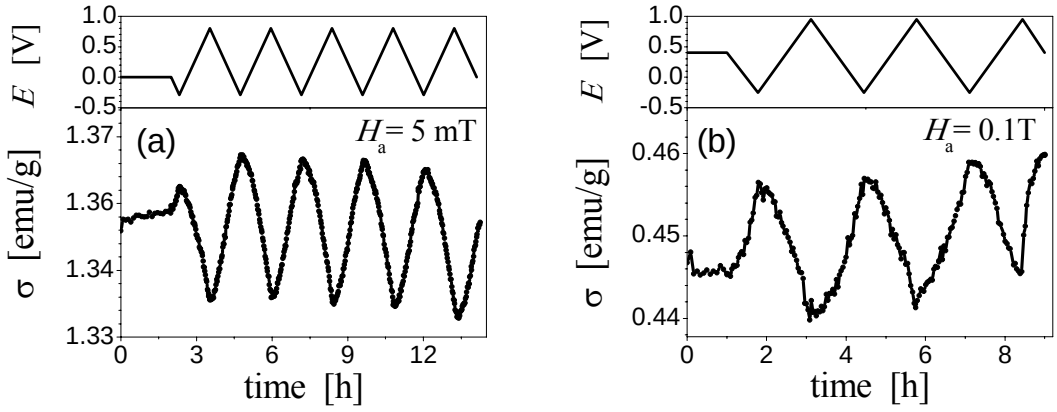

Fig. 3.18: Maximum relative change in magnetization of about (a) 2.35% in $Pd_{60}Ni_{40}$ alloy and (b) 3.14% in $Pd_{89}Co_{11}$ alloy recorded at 5 mT and 0.1 T, respectively.

Considering the peak-to-peak amplitude of the magnetization, a maximum relative change of about 3.14% was recorded in $Pd_{89}Co_{11}$ alloy [Fig. 3.18(a)] and 2.35% in $Pd_{60}Ni_{40}$ [Fig. 3.18(b)] at an applied magnetic field of 0.1 T and 5 mT respectively. These values were estimated after correcting the diamagnetic signal of the background to be discussed in the next page.

The reason for upward (downward) drift in σ may be attributed to a tiny shift (fraction of mm) of the sample position shown in Fig. 3.19. Figure 3.19 corresponds to Fig. 3.18(b). It is emphasized that the change of sample position does not follow a reversible trend, so it cannot affect the reversible variation of σ. Secondly, the peak-to-peak amplitude of σ remains unchanged in spite of the drift. Therefore, shifting of the sample in this small magnitude may be ignored here.

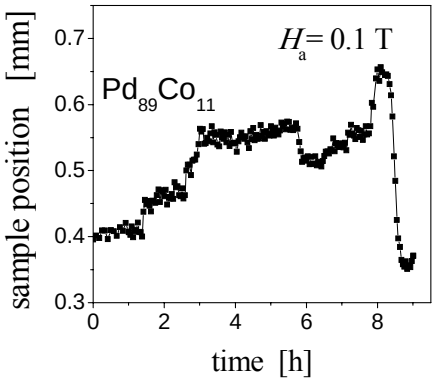

Fig. 3.19: Recorded change of the sample position in (a) $Pd_{60}Ni_{40}$ and (b) $Pd_{89}Co_{11}$ during *in-situ* measurement of magnetization in Fig. 3.18.

The background measurements of the cell (without sample) indicated a diamagnetic signal of the order of 10^{-5} emu at 10 mT to 10^{-2} emu at the maximum measuring field of 8 T as shown in Fig. 3.20. This value is smaller than the sample signal by two to four orders of magnitude. The background signal measured at different magnetic fields was subtracted for estimating the net change of magnetization recorded at the respective magnetic fields.

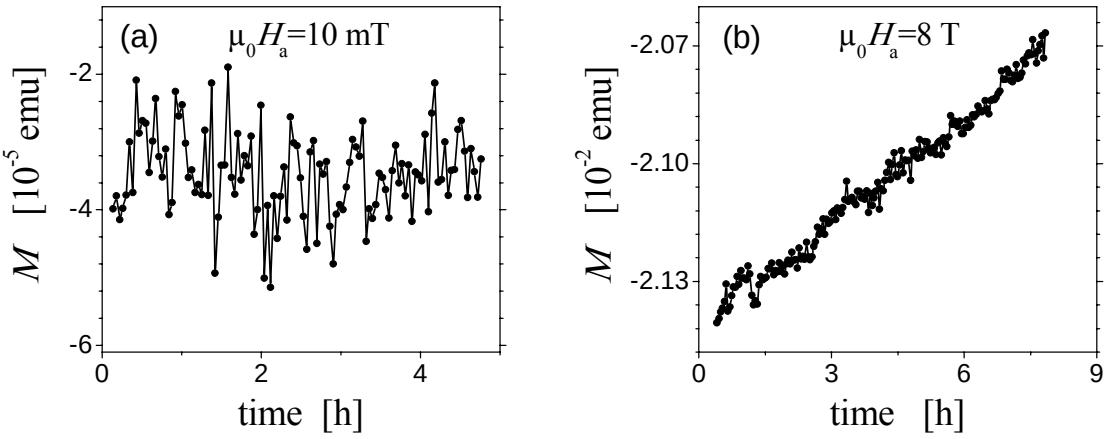

Fig. 3.20: DC measurements performed with electrochemical cell (excluding sample), exhibiting diamagnetic signal of the background at (a) H_a = 10 mT and at (b) maximum measuring field, H_a = 8 T.

The following conclusions can be drawn based on the *in-situ* measurements of magnetization in the non-aqueous electrolyte:

- Observation of the reversible variation of magnetization in both the Pd-Ni and Pd-Co alloy systems.
- Amplitude of the change of magnetization, $\Delta\sigma$, does depend on composition and applied magnetic field.
- Magnetization varies linearly with the excess charge.
- Magnetization-charge coefficient, $\delta M/\delta Q$ in Pd-Ni and Pd-Co alloy systems is of similar magnitude.
- Positive and negative sign of $\delta M/\delta Q$ in Pd-Ni alloys whereas only negative sign of the magnetization in all the Pd-Co alloys.
- $\delta M/\delta Q$ approaches zero in Pd-Ni alloys beyond 1 T field, whereas it shows increasing trend for Pd-Co alloys up to 8 T field.

3.6.2.2 Measurements in aqueous electrolyte

Figure 3.21 shows results of the *in-situ* measurements of magnetization in 1 M KOH solution. A reversible change of magnetization σ was observed on the variation of applied potential, *E*, see Fig. 3.21(a). Considering the peak-to-peak amplitude of σ, a maximum relative change of about 24.8% was obtained in the $Pd_{67}Ni_{33}$ alloy at the measuring field of 5 mT. It was noticed that the maximum change occurs between −0.9 V to −2 V. In this potential range, the voltammogram [Fig. 3.21(b)] also exhibits a fluctuation of the current resulting from the evolution of gas bubbles observed during the *ex-situ* cyclic voltametry studies outside the magnetometer.

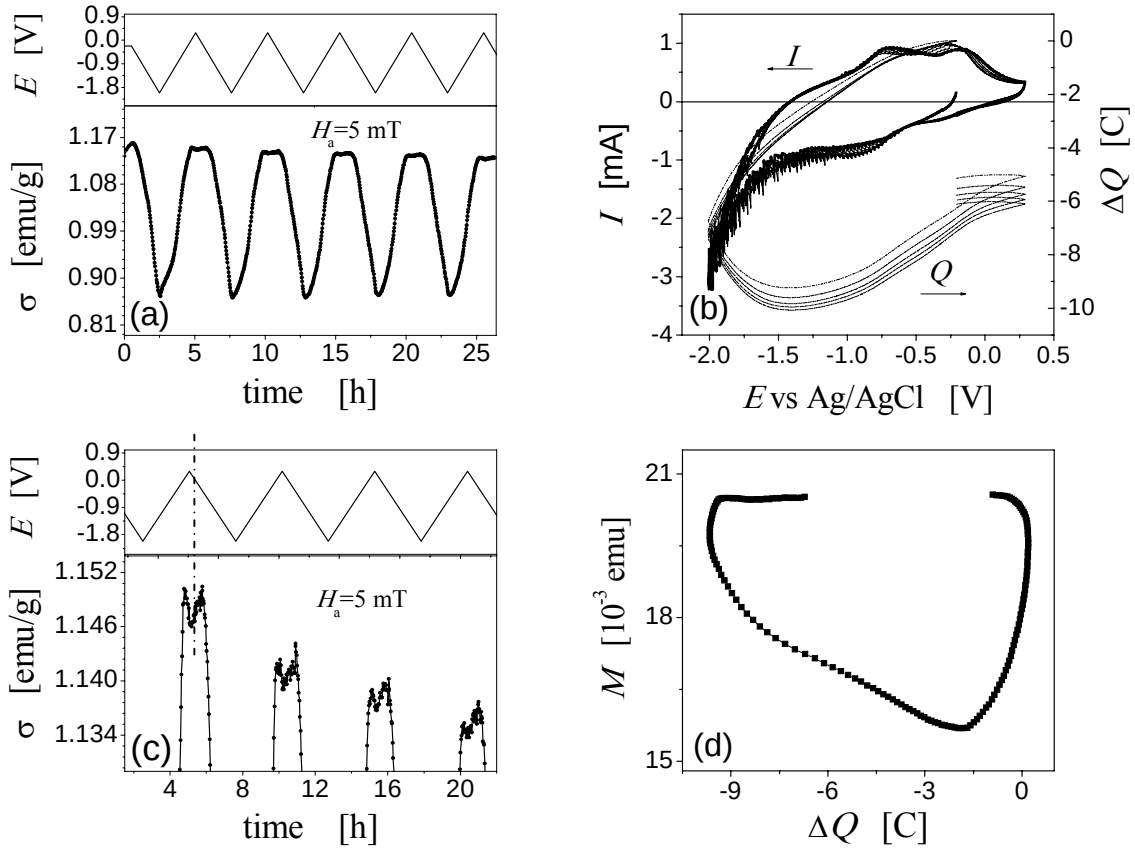

Fig. 3.21: (a) Variation of the mass magnetization, σ, and applied voltage, *E*, in $Pd_{67}Ni_{33}$ alloy at a constant measuring field, H_a = 5 mT. (c) is the zoom image of (a). (b) Cyclic voltammogram recorded during the measurement of σ indicates fluctuation of current (*I*) and charge transfer Δ*Q* on the sample electrode in 1 M KOH solution. The potential scan rate was 0.25 mVs^{-1}. (d) Magnetization, *M*, plotted against Δ*Q*, showing non-linear variation of *M*.

A small plateau of the linear change of σ is apparent in Fig. 3.21(a) which corresponds to the anodic region of the charging, ranging from -0 to 0.3 V. On further zooming into the image of Fig. 3.21(a), it was observed that there exists a small downward peak near $E = 0.3$ V, see Fig. 3.21(c), i.e. a reduction of σ with increasing positive potential.

It has been discussed earlier in section, 4.4.1 that KOH is a strongly adsorbing electrolyte and can oxidise sample at the anodic region of charging (positive-E). Therefore, a possible reason for the small reduction of σ might be attributed to the electrosorption of the antiferromagnetic oxide layer (NiO) on the surface of the $Pd_{67}Ni_{33}$ alloy electrode. On the other hand, the change of magnetization is believed to be the resulting effect of hydrogen adsorption, which has been observed previously in Pd-Ni [52] and also in Pd [53]. As an example, Fig. 3.22 shows that the magnetic susceptibility reduces significantly on the variation of hydrogen content in the bulk palladium.

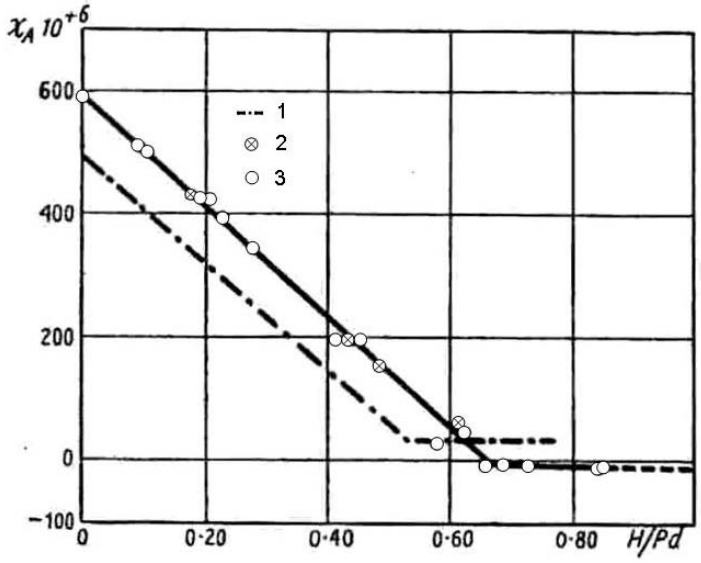

Fig. 3.22: Atomic susceptibility plotted against the ratio of the number of H to the number of Pd atoms, showing decrease of the susceptibility with increase of H content. [1] Aharoni J. Simon F., *Zeits. f. Phys.Chem.* B, **4**, 89-175, 1929. [2] Biggs H. F., *Phil. Mag.* **32**, 40-131, 1916. [3] Svensson B., *Ann. D. Physics*, **18**, 299-304, 1933.

In comparison to the linear variation of magnetization-charge plot [Fig. 3.16(b, d)] in the non-aqueous electrolyte, a non-linear correlation can be seen in Fig. 3.21(d). This is an indication that surface specific adsorption may play a significant role here for the large change of magnetization.

The concluding remarks on the *in-situ* measurements of the magnetization in aqueous KOH solution (adsorbing electrolyte) are as follows:

- Reversible variation of magnetization in Pd-Ni alloy is observed.
- Amplitude of the change of magnetization, $\Delta\sigma$ is nearly 24.8%.
- Magnetization varies non-linearly with charge against linear variation of σ in non-aqueous electrolyte.
- Adsorption of hydrogen plays significant role for the change of magnetization.

3.7 *In-situ* strain measurement

Figure 3.23 shows the results of the *in-situ* measurements of elastic strain during charging of the sample in 1 M $LiClO_4$ in ethyl acetate solution using a small electrochemical cell in the dilatometer.

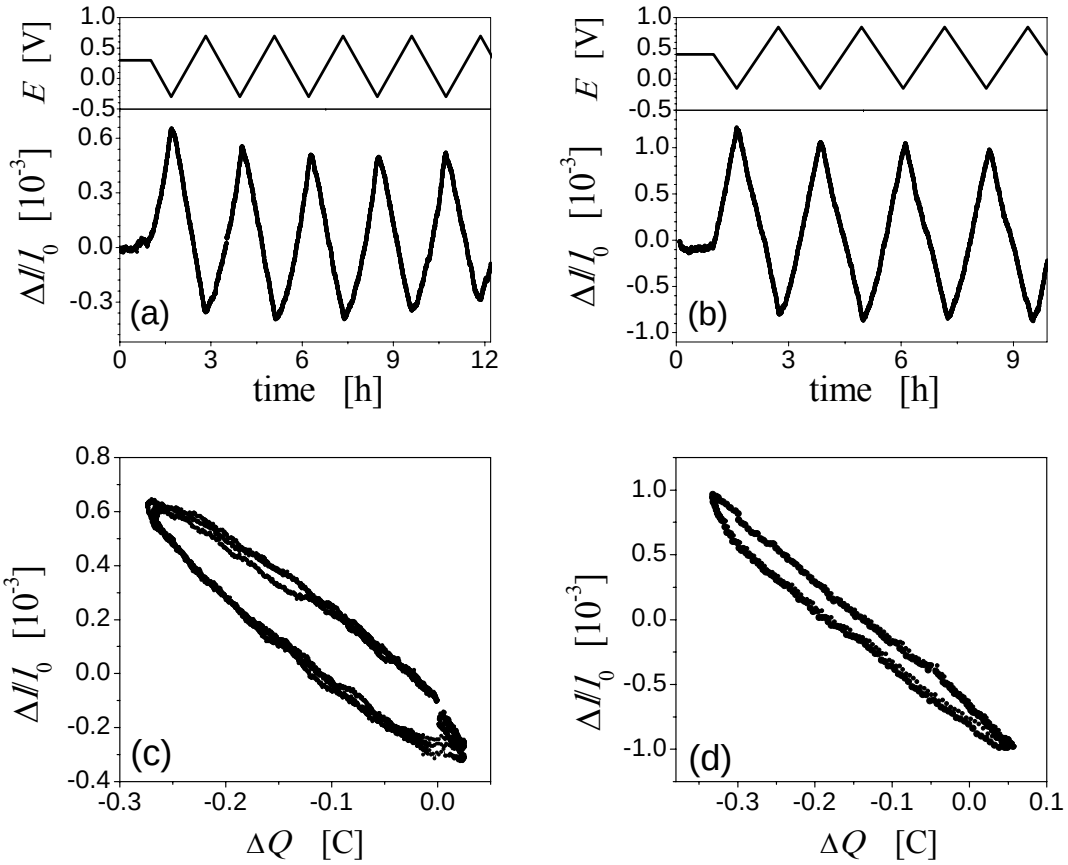

Fig. 3.23: Applied voltage, E and the elastic strain, $\Delta l/l_0$, plotted with time in (a) $Pd_{65}Ni_{35}$ and (b) $Pd_{72}Co_{28}$ alloy, showing charge, ΔQ, dependent variation of $\Delta l/l_0$ in (c) $Pd_{65}Ni_{35}$ and (d) $Pd_{72}Co_{28}$ alloys.

The change of applied potential, ΔE, results in a reversible cyclic variation of the surface charge, ΔQ, and therefore, of the surface stress and of the strain in both the Pd-Ni and Pd-Co alloys as shown in Fig. 3.23 (a, b). The peak-to-peak amplitude of the strain is around 1×10^{-3} for $Pd_{65}Ni_{35}$ and 2×10^{-3} for $Pd_{72}Co_{28}$. The potential window used for the *in-situ* strain measurements is the same as that of the magnetic measurements. The amplitudes of the strain noticed in $Pd_{65}Ni_{35}$ and $Pd_{72}Co_{28}$ is consistent with the strain observed in the other Pd-Ni [50] and Pd-Co alloys [51] respectively, therefore Δl becomes independent of the sample compositions.

The dilatometer strain $\Delta l/l_0$, plotted against charge, ΔQ exhibits linear variation in both alloys. Linear fitting of the plots [Fig. 3.23(c, d)] yields the slope, $(l^{1}\delta l/\delta Q)$. This quantity is required for the estimation of the surface-stress charge coefficient. According to the ref. [54] surface stress-charge coefficient,

$$\varsigma = -\frac{9}{2}\frac{K}{\rho}\frac{m}{l}\frac{\delta l}{\delta Q} \qquad (2)$$

where K is bulk modulus of a sample having length 'l', mass 'm', and density 'ρ'. The surface stress coefficient for $Pd_{65}Ni_{35}$ and $Pd_{72}Co_{28}$ samples are 1.83 V and 2.85 V respectively. Examples for stress-charge coefficients are shown in Table 1, along with the parameters used in the calculation. Consistent results were found for the remaining alloys.

Table 1: Variables used to compute the surface-stress charge coefficient value for Pd-Ni and Pd-Co alloys.

sample	K [GPa]	m [mg]	ρ [g/cm^3]	$l^{1}\delta l/\delta Q$ [C^{-1}]	ς [V]
$Pd_{65}Ni_{35}$	180	9.21	11.29	-0.00278	1.83
$Pd_{72}Co_{28}$	190	8.09	11.45	-0.00473	2.85

The concluding remarks on the *in-situ* measurements of strain in non-aqueous electrolyte are

- reversible variation of strain in Pd-Ni and Pd-Co alloys.
- Total amplitudes of the strain are 1×10^{-3} for $Pd_{65}Ni_{35}$ alloy and 2×10^{-3} for $Pd_{72}Co_{28}$ alloy.

- Strain varies linearly with charge in non-aqueous electrolyte.
- Surface-stress charge coefficient is nearly 1.83 V in $Pd_{65}Ni_{35}$ alloy and 2.85 V in $Pd_{72}Co_{28}$ alloy.

4 Discussion

This section first discusses the microstructure and the magnetic behaviour of the dry samples and then correlates elastic strain to the magnetic measurements in both alloy systems.

4.1 Dry samples: microstructure and magnetic behaviour

The samples presently being used here are loose agglomerates of fine crystals interconnected by metallic grain boundaries as indicated by the high resolution transmission electron microscopy (HRTEM). The size of the crystallites measured by X-ray diffraction analysis is in the range of 6-7 nm. This is in agreement with the TEM analysis. The EDX analysis indicates a variance of the sample composition up to two atomic percent because of the difference in evaporation rate of the alloying elements. Regarding purity of the sample, oxide layer could not be found in the high resolution TEM image and also in the diffraction pattern of the binary Pd-Ni and Pd-Co alloys. Well defined lattice fringes were observed at the surface of the particles [Fig. 3.5]. Hence based on the TEM and X-Ray analysis no indication could be found that would demonstrate an oxidation of the particles.

Hysteresis loops measured with the samples under field and zero field condition of cooling indicated the absence of exchange biasing in both alloy systems. Hence, a core-shell structure [13] may not be expected here or an oxide layer, if present, may be too thin to affect the magnetic measurements [39]. The isotherm of the mass magnetization indicates that samples have low coercivity at room temperature. The temperature-dependent zero-field cooled (ZFC) data indicate that the cusp appears at the temperature at which applied magnetic field nearly equals the coercive field. The inverse susceptibility plotted against temperature [Fig. 3.12(b)] disagrees with the Curie or Curie-Weiss law. So, the presence of a para- or superparamagnetic phase may well be excluded here. The ferromagnetic – as opposed to superparamagnetic – state of the materials is consistent with its microstructure as observed by transmission electron microscopy: multiply branched, contiguous chains of nano-particles exchange coupled by the metallic grain boundaries.

The following conclusions can be made based on the microstructure study and magnetic measurements of the dry samples.

- The samples presently being compacted are the loosely agglomerated nanocrystals of the crystallite size within 6-7 nm.
- The particles are ferromagnetic at room temperature.
- Particles are expected to be free from surface oxide as exchange biasing could not be seen in Pd-Ni and Pd-Co alloys. Neither XRD nor TEM studies could either confirm the presence of any oxide.
- Though the particles are fine, they are not superparamagnetic.

The above conclusion summarizes the fact composition chosen for the present experiments have the Curie temperature above the room temperature. The absence of exchange biasing suggests that they are reasonably stable against the atmospheric effect of the surface oxidation; so it might be safe to use them in electrolyte medium as well.

4.2 Electrochemical process

The cyclic voltammogram recorded with 1 M ethyl acetate solution is the first of its kind in transition metal alloys; therefore, it could not be correlated to any literature. The absence of reaction peaks, and continuous charging and discharging of samples indicates that the sample surface is reasonably clean in ethyl acetate solution.

The cyclic voltammogram shown in Fig. 3.6 indicates that oxidation and hydrogen gas evolution, which might be combined with hydrogen adsorption and absorption, are the dominant electrochemical processes in aqueous KOH. This is in agreement with the literature [44, 45, 46]. However, intentional use of such a reactive electrolyte like KOH may give an insight into changes of the magnetic properties under the condition of specific adsorption at the surface.

The following inferences can be made based on the understanding of electrochemical process in non-aqueous and aqueous electrolytes respectively:

- Both the Pd-Ni and Pd-Co samples are reasonably stable in 1 M ethyl acetate solution. Since the voltammogram lacks any signature of the electrode reaction it can be treated as a weakly adsorbing electrolyte.
- KOH causes oxidation and hydrogenation of the Pd-Ni sample electrodes. It has therefore been considered as a strongly adsorbing electrolyte.

The following section now discusses the relative contribution of both the electrolytes to the change of magnetic properties. The experiments are mainly concerned with the changes of the magnetic properties in low adsorption regime which is main objective of the present work.

4.3 Effect of surface charging on the magnetic properties

4.3.1 Measurements in strongly adsorbing electrolyte

The magnetization in KOH medium started to fall at the onset of the noise (current fluctuation) resulted by the evolution of gas at the cathodic region of the voltammogram. Since palladium has strong affinity for hydrogen, hydrogenation is expected to be the main reason for the large change of magnetization in $Pd_{67}Ni_{33}$ alloy [52, 55]. On the other hand oxidation [44, 45] causes the formation of antiferromagnetic oxide layer, therefore a small reduction in magnetization [Fig. 3.21(c)] at the anodic region of the charging. A compelling argument on the non-linear variation of magnetization with charge [Fig. 3.21(d)] indicates that there are more than one processes is active during cycling of the potential in aqueous electrolyte. So, the change of magnetization in KOH electrolyte is analogous to the modification of sample surface with adsorbent.

4.3.2 Measurements in weakly adsorbing electrolyte

The AC-susceptibility measurements show $\delta\chi'/\delta Q > 0$ only in $Pd_{75}Ni_{25}$ but negative values of $\delta\chi'/\delta Q$ has been found in all the other Pd-Ni and the Pd-Co alloys studied, see Fig. 3.15.

The DC measurements of magnetization exhibits $\delta M/\delta Q > 0$ in $Pd_{1-x}Ni_x$ [x = 26, 33] alloys but $\delta M/\delta Q < 0$ has been found in $Pd_{1-x}Ni_x$ [x = 40, 65] and in all the Pd-Co alloys, see Fig. 3.17. The motivation of the work, which begins with the modification of electronic density of states with the excess charge density, will now be discussed here in the context of band-filling argument.

4.3.2.1 Inspection of band filling

Recently, the influence of surface charging on the paramagnetic susceptibility of Pd has been discussed with respect to the Stoner equation for enhanced paramagnetic susceptibility,

$$\chi = \frac{\mu_B^2 D(E_F)}{1 - 1/2U D(E_F)}, \qquad (3)$$

where $D(E_F)$ is the electronic density of states at the Fermi-edge and $U = 0.789$ eV the effective potential of exchange interaction [56]. μ_B is the Bohr's magneton. Adding of elec-

trons to (withdrawing of electrons from) the nearly filled palladium d-band gives rise to a decrease (increase) of electronic density of states from $D(E_F)$ to $D(E_1)$ [Fig. 4.1(a)]. According to Eq. (3) reduction of $D(E_F)$ with the excess charge, ΔQ means reduction of χ and vice-versa. Therefore, $\delta\chi/\delta Q > 0$, which has been observed in nanoporous Pd [29, 57], see Fig. 4.1(b).

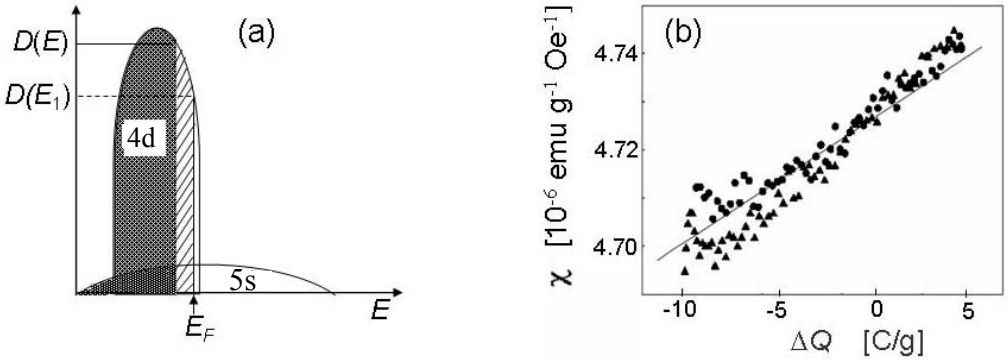

Fig. 4.1: (a) A simplified band diagram showing the change in the electronic density of states, $\Delta D(E) = D(E) - D(E_1)$ with excess charges, ΔQ, resulting (b) $\delta\chi/\delta Q > 0$ in nanoporous Pd [29]. It contrasts with the present experimental results as $\delta\chi'/\delta Q < 0$ and $\delta M/\delta Q < 0$ has been noticed in many of the Pd-Ni and Pd-Co alloys.

It is emphasized that the change of susceptibility for Pd-Ni/PdCo alloys found in the present work [Figs. 3.14(b, d)] is three orders of magnitude higher than that observed for Pd in Ref. [29]. However, the results could not be reconciled with the Stoner model – which has $\delta\chi/\delta Q > 0$ for Pd – because a negative response of the susceptibility to charging was observed in Pd-Co alloys and in majority of the Pd-Ni alloys. The attention is therefore diverted to the other processes, which might explain the change of magnetization or susceptibility in metal-electrolyte composite.

4.3.2.2 Alternative explanations

On the effect of the discussed reversible change of σ and χ', one could associate the change as the selective leaching of Ni or Co atoms from the solid solution. To test this argument, firstly EDX has been taken before and after *in-situ* charging experiments. As an example, a Pd-Co (≈27.5 at% Co) sample shows a change to nearly 27.7 at% Co after a several cycle of charging which is within the error range of the EDX measurement. Nevertheless, if dissolution has to be admitted, no reversible behaviour would be observed. Because of the Gibbs-Thomson-equation [58], nanoparticles are unstable with respect to coarsening (the

so-called Ostwald-ripening): matter dissolved from a nanoparticle will preferentially redeposit elsewhere, forming a single macroscopic particle with lesser surface area and, consequently, lesser free energy. This new particle would have quite different magnetic properties and, most importantly, because of its negligible surface area it would not exhibit significant reversible variation of the magnetization under potential control. To be further confirmed about redeposition, EDX of the counter electrode did not find any trace of elements belonging to the working electrode (sample). Thus, present experimental evidence of stable and reproducible magnetization amplitude over many cycles completely rules out any dissolution-redeposition process during the *in-situ* magnetic measurements.

At the end, to explain the failure of band filling argument, surface specific adsorption or selective dissolution of alloying elements, the attention is diverted to the dimensional changes of the samples resulted by the charge or the charge induced strain or pressure in the transition metal alloys.

4.4 Background: magnetostriction

Magnetostiction [13, 59] is the change of the dimension of a material in response to change of magnetization or the magnetic field. It can be classified as

(1) Spontaneous magnetostriction: It occurs when a ferromagnetic material is cooled from its Curie point, causing dimension change due to ordering of the spins.

(2) Forced magnetostriction: It is associated with the dimension change of a material at large magnetic field i.e., magnetostriction effect near saturation.

Magnetization change observed in a magnetic material under stress is called *inverse* magnetostriction. It includes the combined effect of stress and the magnetic field, and is of relevance in the present context because electrochemical charging leads to substantial amount of strain and stress in the nanoporous materials. The following section now will investigate the effect of strain or stress to the change of magnetization in the Pd-Ni and Pd-Co alloys.

4.4.1 Magnetoelastic effect

The *in-situ* dilatometry studies shown in section 3.7 above revealed a noticeable strain in the transition metal alloys used for the charging experiments. Since the sample is statistically isotropic, the relative volume change, $\Delta V / V$, may be approximated as three times the linear strain, ε. From the peak-to-peak amplitude of ε, the corresponding pressure within the solid can be estimated using the relation

$$P = -3\,\varepsilon K \qquad (4)$$

with bulk modulus $K \approx 186$ GPa and 190 GPa for the respective alloy composition [60]. The maximum amplitude of the charge-induced pressure is about $P = 0.56$ GPa in $Pd_{65}Ni_{35}$ alloy and 1.1 GPa in $Pd_{72}Co_{28}$ alloy.

The excess of charge located at the surface changes the bonding between the surface atoms and generates strain by expansion and contraction of lattice. It has been shown by in-situ X-ray diffraction that the lattice parameter, a, changes, causing a considerable amount of lattice strain, $\Delta a/a$, in nanoporous platinum during the variation of electric potential in an electrolyte medium [16], see Fig. 4.2(a). Experiments investigating the effect of surface charging on the bonding of surface atoms show that atoms located at the surface are most strongly affected by the surface charge under the conditions of negligible adsorption [16, 61], see Fig. 4.2(b). Since the atoms in a lattice are interconnected by the bonding forces, the strain, which originates at the surface, gets transmitted into the bulk by the network of atomic bonding. As a result, the whole body of a nanoporous material may expand and contract elastically in response of the elastic strain or the strain induced pressure.

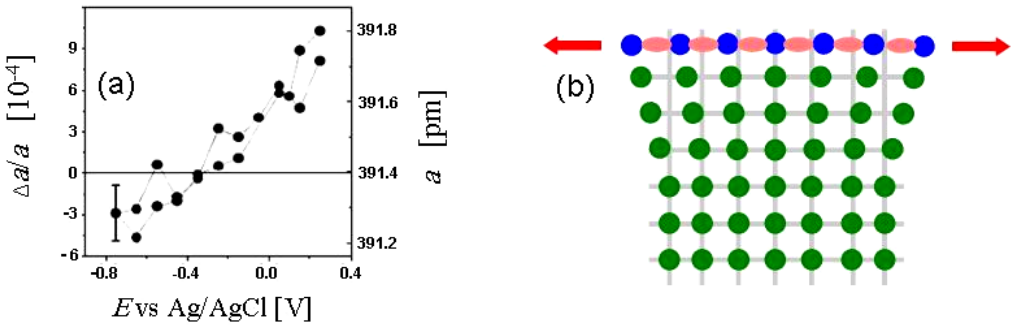

Fig. 4.2: (a) Experimental evidence showing change of the lattice constant, a, and of strain, $\Delta a/a$ on the variation of applied potential, E, in nanoporous platinum measured by *in-situ* X-Ray diffraction study [16]. (b) Schematic diagram, showing a strain originated at the surface due to change in surface stress. Blue colour represents the atoms located at the surface and green colour for the atoms located within the bulk.

If stresses within the bulk and at the surface of a solid are equilibrated, the following capillary equation holds [62, 63]

$$3\ V\langle P\rangle_v = 2\ A\langle f\rangle_A \qquad (5)$$

where f is the surface stress, which is defined as the derivates of the surface tension with respect to strain, V is the total volume of grain, A is the total surface area, $\langle P\rangle_v$ is the

volumetric average of the pressure in the bulk, and $\langle f \rangle_A$ is the mean surface stress, i.e. the area-weighted average of the surface stress of all interfaces, irrespective of geometry and the microstructure. When f becomes tensile, the compensating bulk stress is compressive, and the material contracts. For a nanoporous material, which has high surface to volume ratio interface stress varies linearly with the variation of superficial charge density, resulting in a significant elastic deformation of the samples as observed previously in non-magnetic samples [16, 24, 64].

Often, the surface stress varies linearly with the superficial charge density; see e.g. the results of [16, 24, 54, 61] and the calculations in [64]. For this linear case, the derivative $\varsigma = \mathrm{d}f/\mathrm{d}q$, the surface stress-charge coefficient, is the most important material parameter to describe the corresponding phenomena at the metal-electrolyte interface. Sign and magnitude of ς vary depending on the electrochemical processes at the metal surface, and therefore, on the type and concentrations of the substances which are present. The quantity, ς is therefore a characteristic material property of an electrode-electrolyte interface.

Besides affecting the in-plane forces at the surface, which are quantified by the surface stress, charging will also induce a reversible out-of-plane deformation. This 'surface stretch' [63] takes the form of a relaxation of – essentially – the outermost atomic layer of atoms relative to the first subsurface layer. For values of q characteristic of double-layer charging, the relative change in interplanar spacing can exceed 1% [64].

So far, experiments have found that, upon positive charging, the surface stress generally leads to a volume expansion (negative pressure) in the bulk, and the stretch is negative (inward relaxation) at the surface [16, 24, 63, 65]. Both modes of relaxation may affect the magnetization, in the bulk and/or at the surface, via the magnitude of the atomic magnetic moment, the exchange interaction, and/or the magnitude and direction of the magnetic anisotropy.

In view of the significant effect of charge on the lattice deformation, it is of interest to plot the charge-induced change in magnetization versus the pressure. Differentiating Eq. (4) for P with respect to Q provides,

$$\frac{\mathrm{d}P}{\mathrm{d}Q} = -3K\left(\frac{\mathrm{d}\varepsilon}{\mathrm{d}Q}\right), \tag{6}$$

so that

$$\frac{\mathrm{d}\sigma}{\mathrm{d}P} = \left(\frac{\mathrm{d}\sigma}{\mathrm{d}Q}\right)\left(\frac{\mathrm{d}P}{\mathrm{d}Q}\right)^{-1} = -\frac{1}{3K}\left(\frac{\mathrm{d}\sigma}{\mathrm{d}Q}\right)\left(\frac{\mathrm{d}\varepsilon}{\mathrm{d}Q}\right)^{-1}. \tag{7}$$

In the present experiments, $\delta\varepsilon/\delta Q$ was evaluated from the slope of graphs such as Figs. 3.23(c, d). Substituting this value in Eq. (6) provides $\delta P/\delta Q$. Furthermore, $\delta\sigma/\delta Q$ was obtained from the slope of Figs. 3.16 (b, d), correlating (mass) magnetization with the excess charge, ΔQ. Using these experimental values with Eq. (7) yields a magnetization-pressure coefficient, $\delta\sigma/\delta P$, as shown in Fig. 4.3(a). It is also of interest to inspect the same information from a slightly different angle, namely after normalization to the magnetization. This is represented by the parameter $\sigma_A^{-1}\delta\sigma/\delta P$, see Fig. 4.3(b).

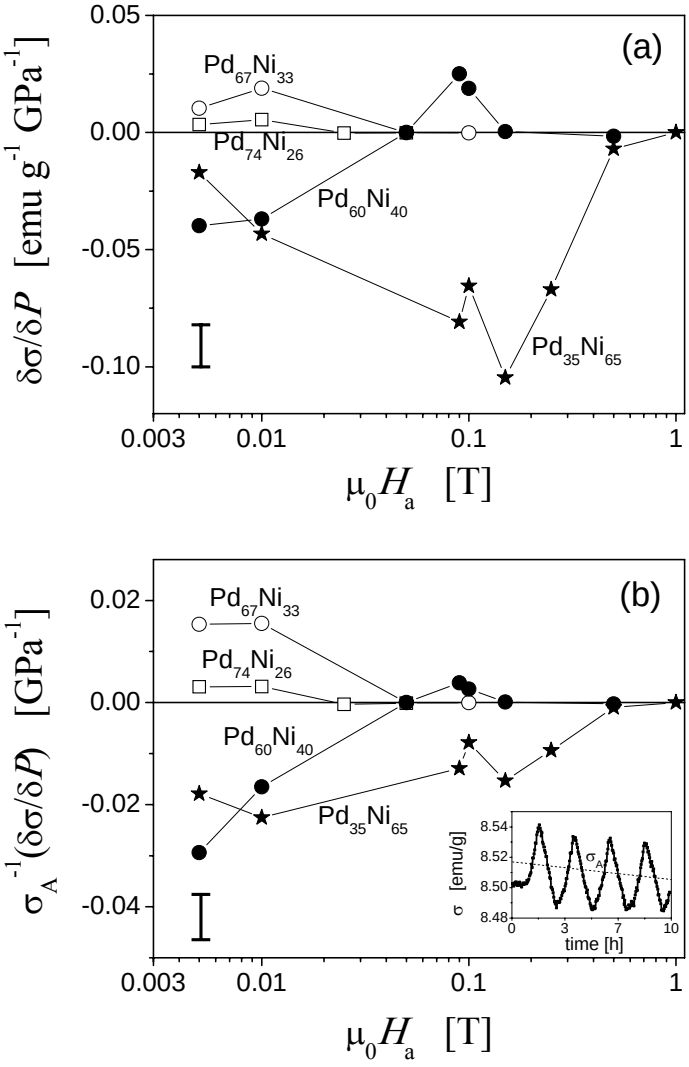

Fig. 4.3: (a) Field dependent variation of magnetization-pressure coefficient, $\delta\sigma/\delta P$ normalized to (b) $\sigma_A^{-1}\delta\sigma/\delta P$ after dividing $\delta\sigma/\delta P$ with σ_A. Dotted line indicating σ_A at the inset of (b).

The quantity σ_A represents the (average) absolute value of σ at the respective field, as illustrated in the inset of Fig. 4.3(b). Figure 4.4 shows the analogous information for the Pd-Co samples.

The net error bars for $\delta\sigma/\delta P$ (see Figs. 4.3(a) and 4.4(a)) are dominated by the error in ε versus Q, as obtained from the standard deviation of the linear fit in graphs such as Fig. 3.23. A lesser important contribution arises from the estimation of σ_A.

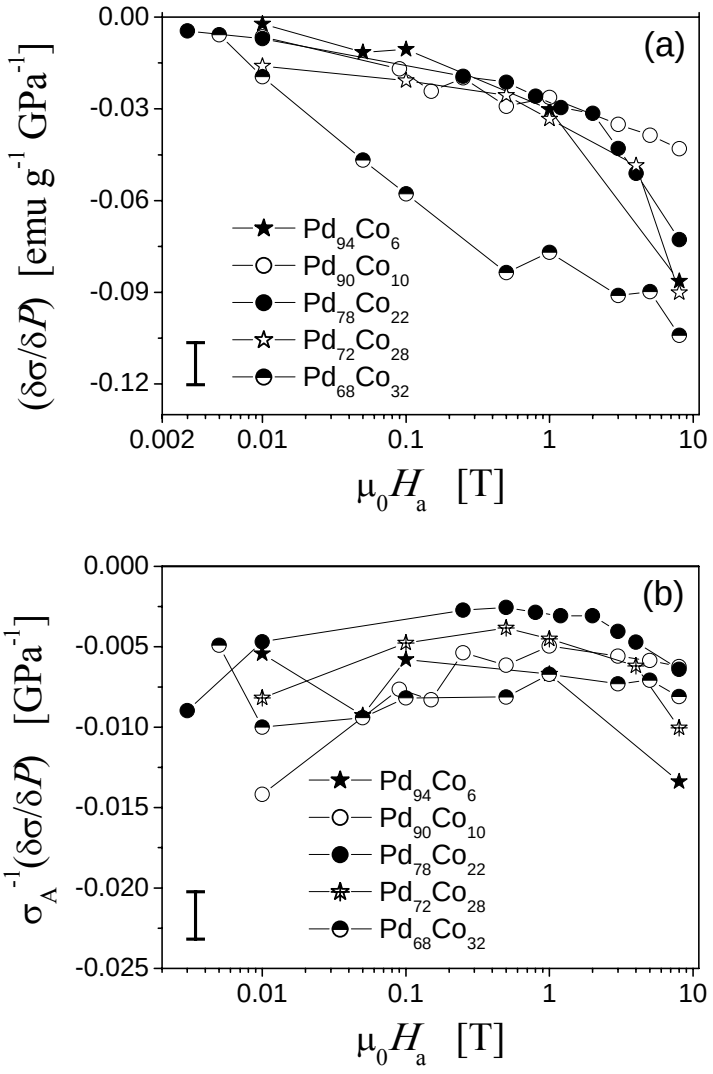

Fig. 4.4: (a) Experimental data obtained from *in-situ* measurement of strain and magnetization at 300 K. Resulting plot (b) obtained by dividing σ_A to $\delta\sigma/\delta P$, showing tendency to merge into a constant value.

Figures 4.3 and 4.4 summarize an essential part of the results of the present work. Because the δP scale essentially with the δQ, the graphs also represent – qualitatively – the charge dependence of the magnetization, see Fig. 3.17 above for a quantitative plot. By inspection, the following observations are made:

- For Pd-Ni, the $\sigma^{-1}\delta\sigma/\delta P$ (as well as the $\sigma^{-1}\delta\sigma/\delta Q$) are finite at small applied field, and they tend to zero at applied field values around 1T.
- By contrast, the analogous coefficients for Pd-Co are essentially independent of H_a. In particular, they retain finite values even at $\mu_0 H_a$ as large as 9T.
- As an additional distinction, the $\sigma^{-1}\delta\sigma/\delta P$ and $\sigma^{-1}\delta\sigma/\delta Q$ for Pd-Ni may be positive or negative in sign, dependent on the alloy composition. By contrast, the analogous quantities for Pd-Co are negative-valued at all compositions studied.

We shall now discuss these findings with relation to two idealized pictures, which examine different aspect of the coupling between pressure and magnetization. The first will assume that the pressure acts exclusively to change the magnetic anisotropy and, thereby, the *orientation* of the spins. Here, the value of $\sigma^{-1}\delta\sigma/\delta P$ vanishes at large H_a, where the anisotropy field becomes insignificant relative to the applied field. This picture agrees qualitatively with the findings for Pd-Ni. The second picture is inspired by the finding that, for Pd-Co, $\sigma^{-1}\delta\sigma/\delta P$ remains finite even at large values of H_a. This cannot be explained by the effect of the pressure on the anisotropy, and it suggests that the pressure changes the *magnitude* of the magnetic moment. This phenomenon is embodied in the coefficient of forced magnetostriction, which connects to the observations in Pd-Co.

4.4.2 Inspection in the context of Stoner-Wohlfarth model

It is well known, that hydrostatic pressure affects the magnetic properties of solids [11, 66, 67]. In particular, it has been reported that hydrostatic pressure acting in Pd-Ni and Pd-Co alloys can affect both the magnetization and susceptibility due to change in exchange energy and anisotropy of the system [66, 68, 69, 70]. Here, we concentrate on the effect on the magnetic anisotropy.

In order to verify ramifications of the effective change of the anisotropy on the net magnetization of an array of magnetic particles with randomly oriented easy axes, a hypothesis based on the Stoner-Wohlfarth model [71] can be discussed here. We assume crystals having anisotropy in random directions, as shown in Fig. 4.5.

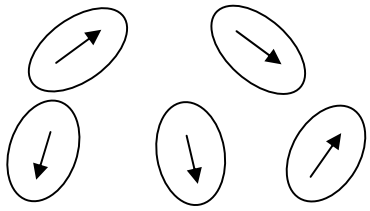

Fig. 4.5: Randomly oriented isolated crystals showing spins along their easy axis in the absence of magnetic field.

The magnetization isotherm, $M(H)$ indicated by the Stoner-Wohlfarth model increases monotonously starting from remanence, like a typical $M(H)$ curve - see Fig. 4.6(a).

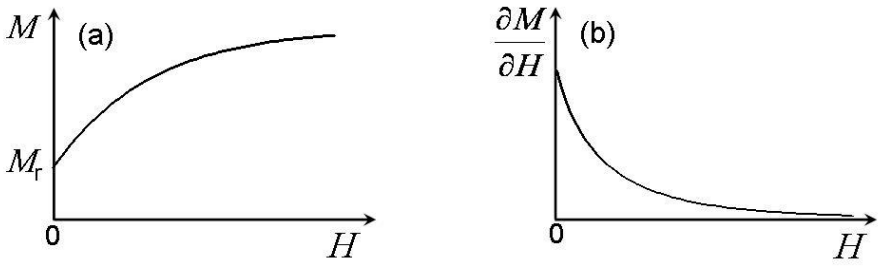

Fig. 4.6: (a) Typical magnetization plot for a ferromagnetic material showing monotonous decrease of magnetization, M with applied field, H until remanence. (b) $\partial M/\partial H$ approaches zero at H tends to be infinity.

The notion of anisotropy behind the Stoner-Wohlfarth model is that each crystal has an 'anisotropy field', $\mathbf{H}_a$. It is a vector which points into the direction of the easy axis and its magnitude measures the strength of anisotropy. If magnetic field is applied along the direction shown in Fig. 4.7, at equilibrium, the magnetization in each crystallite simply points into the resultant direction of the **H** vector and $\mathbf{H}_a$ vector.

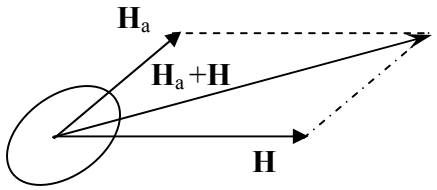

Fig. 4.7: Anisotropy field, $\mathbf{H}_a$, and magnetic field, **H**, applied on a typical isolated crystal. The magnetization is directed along the resultant field, obtained from the vector sum of the two fields: $\mathbf{H}_{Net} = \mathbf{H}_a + \mathbf{H}$.

Within the frame of the Stoner-Wohlfarth model, the action of pressure cannot be to turn the anisotropy field away from an easy axis direction because pressure is a scalar, it has no directionality. The only thing the pressure may do is to change the magnitude, H_a, of $\mathbf{H}_a$. That is how surface charging enters our inspection of the Stoner-Wohlfarth model: we take H_a to be a function of P (or Q). The important materials constant is then dH_a/dP. In the Stoner-Wohlfarth model [71], $M=M(h)$ where $h=(H/H_a)$. Now

$$\frac{dM}{dP}=\left(\frac{dM}{dh}\right)\left(\frac{dh}{dP}\right) \tag{8}$$

and

$$\frac{dh}{dP}=\frac{d\left(H/H_a\right)}{dP}=-\left(\frac{H}{H_a^2}\right)\left(\frac{dH_a}{dP}\right) \tag{9}$$

Combining Eq. (8) and (9),

$$\frac{dM}{dP}=-\left(\frac{H}{H_a^2}\right)\left(\frac{dH_a}{dP}\right)\left(\frac{dM}{dh}\right). \tag{10}$$

Here, H_a and dH_a/dP may be taken as constant. dM/dh is always positive and its magnitude decreases with increasing field. Now, the following information can be obtained:
a) If it is assumed that the decrease of dM/dh is faster than $1/H$, the Stoner-Wohlfarth model should have an at least $1/H^3$ (or faster) variation of dM/dP [Eq. 10], and it converges to zero at large H, see Eq. (11) below.

Considering the Stoner-Wohlfarth model with H along the z axis and $H >> H_a$, then net field vector, H_{Net} in any particular crystallite, to which the magnetization is locally parallel, has approximately the following form:

$$H_{Net} = \{0, H_{a,\,p}, H\}$$

where $H_{a,\,p}$ is the normal component of H_a in that crystallite. $H_{Net,}$ is at an angle $\theta = H_{a,\,p}/H$ to the field, and so is the magnetization. But the magnetization component along the field direction is

$$M=M_S\cos\theta=M_S\left(1-\frac{\theta^2}{2}\right)=M_S\left[1-\frac{1}{2}\left(\frac{H_{a,p}}{H}\right)^2\right]$$

Now, differentiating M with respect to H provides,

$$\frac{\mathrm{d}M}{\mathrm{d}H} = \frac{M_\mathrm{S}\, H_{\mathrm{a,p}}^2}{H^3}\,. \tag{11}$$

b) Since dM/dh is finite as H tends to zero, dM/dP goes to zero at H = 0 and H = very large. Therefore, two zeros of dM/dP are possible in-between a maximum. The experiment shows this trend in $Pd_{35}Ni_{65}$ [Fig. 4.3(a)], and the trend for dM/dP approaches to zero at large field has been elucidated here for all the Pd-Ni samples.

c) On the other hand Pd-Co data shows dM/d$P \approx$ constant at all the field. The following effect would find consistency with the Stoner-Wohlfarth model here if one considers dM/dh proportional to 1/h at large field. However, micromagnetism [72] does not provide any example for such behavior, rather it suggests the following relation for the variation magnetization, M; with the saturation magnetization, M_s

$$\frac{M}{M_\mathrm{S}} = \left(1 - \frac{a}{H^{n/2}}\right) \tag{12}$$

where 'a' is a constant and n - the dimensionality of the perturbing field feature - takes the values 1,2,3,4 for point, line, area, and extended defects. Now, considering n = 1 for slowest approaches to saturation, and differentiating M with respect to H provides, dM/dH proporonal to $H^{-3/2}$. Therefore, dM/dh proportional to 1/h appears unlikely, and hence the Stoner model is poorly adapted to explaining the observations for Pd-Co alloys.

4.4.3 Magnetostriction effect

Having inspected the consequences of the pressure on the magnetic anisotropy, we now turn to the effect of pressure on the magnetic moment. As we shall see, the literature data on the materials behaviour of (conventional, bulk) Pd-Ni in this regards also connects to the observation of the sign change of the magnetization-charge or magnetization-pressure responses in the nanoporous samples. A relevant materials parameter is here the forced magnetostriction coefficient, $\partial\omega/\partial H$, where ω refers to the volumetric strain. Forced magnetostriction is related to another relevant parameter, the volume inverse magnetostriction (i.e., the change of mass magnetization with the pressure), $\partial\sigma_\mathrm{S}/\partial P$, according to [73]

$$\frac{\partial \omega}{\partial H} = -\rho\left(\frac{\partial \sigma_S}{\partial P}\right), \tag{13}$$

where ρ is the bulk density and $\partial\sigma_S/\partial P$ is the change of mass magnetization with the pressure, P. The volume inverse magnetostriction is closely related to the present results for $\delta\sigma/\delta P$, as shown in Fig. 4.3 above.

Figure 4.8 shows values of forced magnetostriction for bulk Pd-Ni alloys from Ref. [73]. It is seen, that $\partial\omega/\partial H$ changes sign with the change of temperature or composition in these materials.

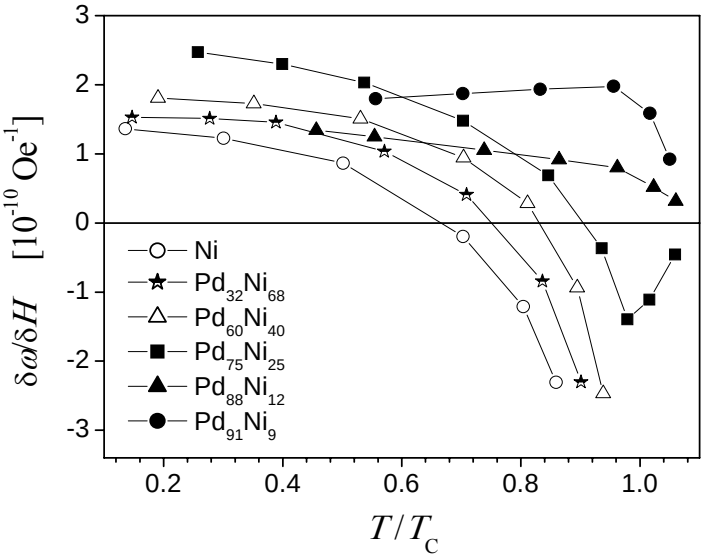

Fig. 4.8: Forced volume magnetostriction, $\partial\omega/\partial H$ with reduced temperature, T/T_C in bulk Pd-Ni alloys where ω is the volumetric strain and H is the applied field, Ref. [73].

With the help of Eq. (13), and using data for the density of the respective alloys, the data in Fig. 4.8 can be converted to $\partial\sigma_S/\partial P$. The result is shown in Fig. 4.9(a). The temperature parameter of Fig. 4.8, which is normalized to T/T_C, can be converted to the absolute temperature scale, using composition dependent T_C of various samples from Ref. [35] (compare Fig. 1.4). For better comparison to the experimental data, the original data of Ref. [73] have been interpolated to obtain a graph for the composition $Pd_{67}Ni_{33}$. This graph is also shown in Fig. 4.9(a).

In an experiment, performed at constant temperature, T a sign change is expected, as indicated by the intersections of the dashed line at $T = 300$ K: the high concentration Ni

sample intersects with the negative part of the $\partial\sigma_S/\partial P$ curve, and the low concentration Ni sample with the positive one. It is noteworthy that the magnetocrystalline anisotropy constant of the Pd-Ni alloy also exhibit sign change depending on the concentration of the alloying elements [74].

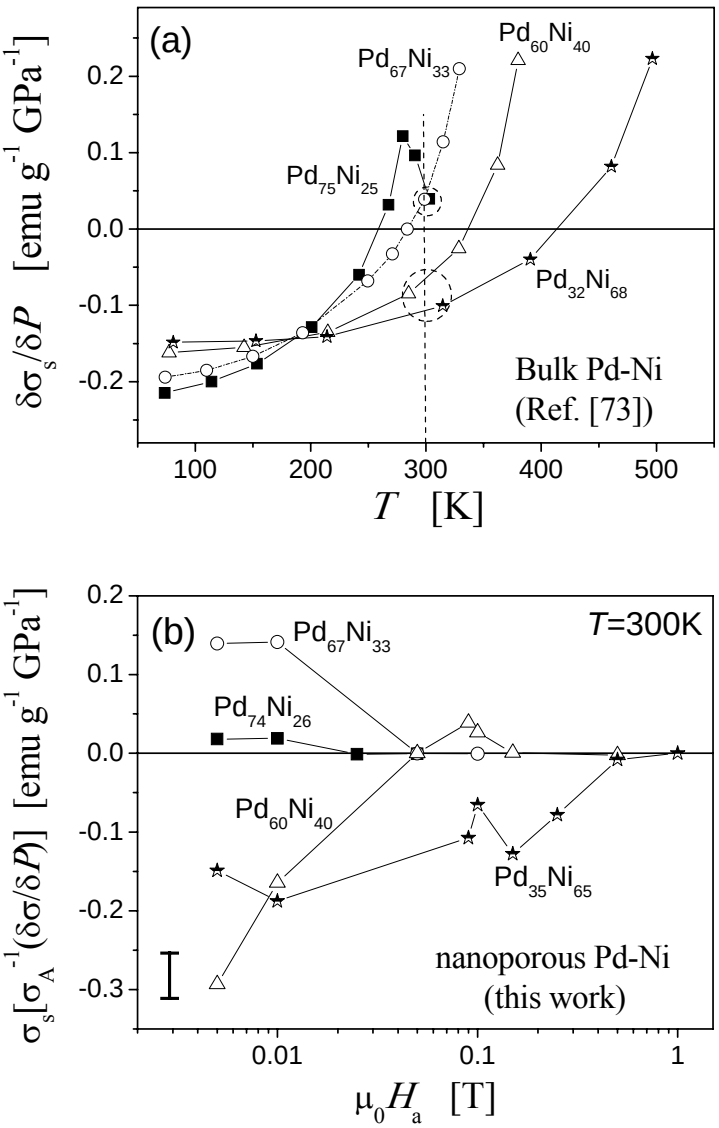

Fig. 4.9: (a) Temperature dependent magnetization-pressure coefficient, $\partial\sigma_S/\partial P$ derived from forced magnetostriction plot of Tokunaga *et. al.* [73] in conventional bulk Pd-Ni alloys. (b) Experimental data obtained from *in-situ* measurements of strain and magnetization of nanoporous Pd-Ni alloys at 300 K, showing a magnitude which is consistent with bulk Pd-Ni.

Figure 4.9(a) is applicable for a sample near saturation, whereas present experiments were performed with samples below saturation. Assuming that the deviation from saturation arises exclusively from the spin misorientation, as opposed from variation of the moment per atom, the effect of pressure - along with forced magnetostriction - on the net magnetization will simply scale with the magnetization itself. Therefore, $\sigma_A^{-1}\delta\sigma/\delta P$ was multiplied with the saturation magnetization (σ_S) of the nanoporous samples in Fig. 4.9(b) for comparison with the literature data. By comparing Fig. 4.9 it can be inferred that the experimental change in the magnitude of the moment and its sign of Fig. 4.9(b) agrees, by order of magnitude, with the data for bulk Pd-Ni [Fig. 4.9(a)].

No forced magnetostriction data appears to be known for Pd-Co. Yet, the data for this alloy are in remarkable agreement with the present argument, inasmuch as $\sigma_A^{-1}\delta\sigma/\delta P$ is a constant, independent of the applied field (compare Fig. 4.4 (b)).

A sign change similar to that in Pd-Ni may not be possible in Pd-Co alloys as reported by Fujiwara *et. al.* [75]. Gontarz *et. al.* [76, 77] noticed that change of magnetic moment is also possible in Pd-Co on account to strain or pressure induced anisotropy of the system at 300 K temperature. We note that the sign of the magnetostriction constant is negative up to 40 at.% of Co in the bulk Pd-Co alloys [78]. The magnetocrystalline anisotropy energy coefficient of the Pd-Co alloys is also negative within the present range of composition [75].

4.4.4 Stoner-Wohlfarth model versus forced magnetostriction

The *in-situ* measurement of magnetization was first discussed with relation to the Stoner equation, in analogy to a previous argument for enhanced paramagnetic susceptibility in nanoporous Pd. The idea of changing the moment per atom through d-band filling is a basic concept to be applied to ferromagnets. However, this argument cannot explain the complex phenomenology of our observations.

The apparent failure of the band filling arguments direct attention to the indirect effect of the charge, i.e. a response of the magnetization via the charge-induced pressure as an intermediate effect. We have discussed this type of mechanism in relation to two alternative approaches: one based on the Stoner-Wohlfarth model for disordered arrays of nanoparticles and the second based on the forced magnetostriction.

The Stoner-Wohlfarth model discusses the magnetization-pressure response with respect to pressure-induced changes of the magnitude of the magnetocrystalline anisotropy. This fits the general phenomenology of the Pd-Ni alloys, though no quantitative comparison is possible for lack of data on pressure-dependent magnetic anisotropy in bulk Pd-Ni. By contrast, the argument is poorly compatible with the observations for Pd-Co. Here, we find better agreement with the second model, which focuses on the effect of the charge-

induced pressure on the magnitude of the magnetic moment per atom. Again, the lack of data on forced magnetostriction in the respective alloys prevents a quantitative comparison. For Pd-Ni, where forced magnetostriction data are available, there is agreement in relation to the magnitude of the magnetization-pressure response. However, the field dependence is here more suggestive of the Stoner-Wohlfarth type model. It must be concluded that, in general, both effects may contribute simultaneously and with comparable magnitude.

5 Summary and Conclusions

The experimental observation of tunable magnetic properties in transition metal alloys by electrochemical charging is the first of its kind. This provides an insight on the possibilities of changing the ferromagnetic ordering without altering the composition or temperature of the specimen. The following inferences can be drawn based on the *in-situ* surface charging experiments performed with nanoporous Pd-Ni and Pd-Co alloy powders.

- A reversible variation in magnetization and susceptibility was observed both in Pd-Ni and Pd-Co nanoporous alloys by a cyclic variation of the applied potential.
- A linear correlation between the magnetization /susceptibility and the excess surface charge indicate that surface specific adsorption was not dominant in non-aqueous electrolyte.
- A reversible variation of about 3% in mass magnetization of $Pd_{89}Co_{11}$ alloy at an applied field of 0.1T was obtained whereas a variation of about 2.3% in $Pd_{60}Ni_{40}$ alloy at 5mT was observed.
- Maximum amplitude of about 1% variation in AC-susceptibility of $Pd_{35}Ni_{65}$ and $Pd_{72}Co_{28}$ were observed
- Magnetization-charge coefficient, $\delta M/\delta Q < 0$ or > 0 was observed in Pd-Ni alloys during variation of measuring field or sample composition whereas $\delta M/\delta Q < 0$ was observed in Pd-Co alloys irrespective of sample composition and magnetic field.
- Negative sign of magnetization contradicts band filling by the extra charge density.

The following inferences can be drawn based on the *in-situ* dilatometry study of strain with nanoporous Pd-Ni and Pd-Co alloy powders.

- A relative variation of 0.1% and 0.2% length change was observed due to electrochemical charging of the samples. It contributes to the elastic deformation and therefore, affecting magnetoelasticity of the Pd-Ni and Pd-Co alloys.

- Hydrostatic pressure ranging from 0.5 to 1 GPa was observed in the Pd-Ni and Pd-Co alloys respectively by the dilatometry experiments.
- The sign and the magnitude of the moment agree well with the literature values of volume inverse magnetostrictive change in Pd-Ni alloys.
- The negative sign of $\mathrm{d}M/\mathrm{d}Q$ in Pd-Co alloys may be related to negative magnetostriction constant as well as magnetocrystalline anisotropy energy of the system.

The motivation of the present work though began with modification of electronic density of states with the excess charge density the present set of experiments suggests that filling (depleting) of d-band may not be possible here. On the contrary, it was found that magnetoelastic response of the transition metal alloys can be affected considerably by the hydrostatic pressure in a metal-electrolyte composite. A quantitative agreement of the experimental data with inverse magnetostriction effect and inspection of the Stoner-Wohlfarth model finally conclude that strain or strain induced pressure could be a driving force for the reversible changes of the magnetic properties in the transition metal alloys.

6 Outlook

The present experimental work is an endeavor to study the charge-induced magnetic properties of transition metal alloys wetted by an electrolyte. A variation of the magnetization of up to 3% has been observed in non-aqueous electrolyte and the effect has been explained by the charged-induced strain. Three main things might be done in the future:

1) Systematic studies of the electrochemical processes with X-Ray photoelectron spectroscopy or electrochemical impedance spectroscopy. Since 1 M ethyl acetate solution has been used here for the first and currently no literature is available, it will always be worthy to find a demarcation line between so called double layer regime and adsorption regime for further use of this electrolyte. Eventually, a larger potential window may come out and possibly a large change of the magnetization than small potential window used here. At the same time one may search for a new electrolyte which may provide larger potential for enhancing the relative amplitude of the change above 3%.

2) An *in-situ* measurement (e.g. by NEXAFS) of the electronic density of states during electrochemical charging of the samples may confirm the effect of pressure to the empty states of the d-band transition metal alloys. The work may be supported by theoretical calculations as well.

3) In order to distinguish the effect of pressure and the charge, a similar set of experiments can be performed with thin film samples. Due to constrain of the film with substrate the effect of pressure would be negligible. In that case resulting effect of the charge will come into the picture.

4) Another field of interesting research would be to find materials for which the effect is even stronger than the one observed here. The ultimate goal would be to find a material which could be switched cyclically between the ferromagnetic and the paramagnetic state just by applying a voltage.

References

[1] Gleiter H., *Acta Mater.*, **48**(1), 1-29, 2000.

[2] Gleiter H., *Prog. Mater. Sci.*, **33**, 223-315, 2000.

[3] Cao G., *Nanostructures & Nanomaterials: Synthesis, Properties & Applications*, Imperial College Press, 2004.

[4] Huaizhi Z., Yuantao N., *Gold Bulletin*, **33**(3), 103, 2000.

[5] Chen M. S., Goodman D. W., *Catalysis Today*, **111**(1-2), 22-33, 2003.

[6] Youssef K. M., Scattergood R. O., Murty K. L., Horton J. A., Koch C. C., *Appl. Phys. Lett.*, **87**, 09190,2005

[7] McFadden S. X., Mishra R. S., Valiev R. Z., Zhilyaev A. P., Mukherjee A. K., *Nature*, **398**, 684, 1999.

[8] Bregliozzi G., Schino A. D., Ahmed S. I.-U., Kenny J. M., Haefke H., *Wear*, **258**, 503-510, 2005.

[9] Magness I., Kecskes L., Chungs M., Kapoor D., Biancianello F., Ridder S., 19th *International Symposium of Ballistics*, Switzerland, 1183, 2001.

[10] Karch J., Birringer R., Gleiter H., *Nature*, **330**, 556-558, 1987.

[11] Michels D., Krill C.E., Birringer R., *J. Mag. Mag. Mater.*, **250**, 203, 2002.

[12] Herzer G., *IEEE Transaction on Magnetics*, **26**(5), 1397-1402, 1990.

[13] Cullity B. D., *Introduction to Magnetic Materials*, Addition-Wesley Publishing Company, 1972.

[14] Volker Z., Jürgens B., Schultz C., Biener J., Biener M. M., Hamza A. V., Bäumer M., *Angewandte Chemie-International Edition*, **45** (48), 8241-8244, 2006

[15] Biener J., Hodge A. M., Hayes J. R., Volkert C. A., Zepeda-Ruiz L. A., Hamza A. V., Abraham F. F., *Nano Letters*, **6**(10), 2379, 2006.

[16] Weissmüller J., Viswanath R. N., Kramer D., Zimmer P., Würschum R., *Science*, **300**, 312-315, 2003.

[17] Gleiter H., Weissmueller J., Wollersheim O., Wuerschum R., *Acta Mater.*, **49**, 737-745, 2001.

[18] Zhang Z., Wu F., Lagally M. G., *Annu. Rev. Mater. Sci.*, **27**, 525, 1997.

[19] Fichtner M., *Advanced Engineering Materials*, **7**(6), 1-13, 2005.

[20] Monk P. M. S., *Fundamentals of Electroanalytical Chemistry*, Wiley, 2001.

[21] Greef R., Peat R., Peter L. M., Pletcher D., Robinson J., *Instrumental Methods in Elelctrochemistry*, edited by Kemp T. J., 1986.

[22] Tucceri R., *Surface Science Reports*, **56**, 85-157, 2004.

[23] Lust E., Jänes A., Arulepp M., *J. Electroanal. Chem.*, **512**, 33-42, 2004.

[24] Kramer D., Viswanath R.N., Weissmüller J., *Nano Letters*, **4**, 793-796, 2004.

[25] Sagmeister M., Brossmann U., Landgraf S., Wuerschum R., *Phys. Rev. Lett.*, **96**, 156601, 2006.

[26] Baughman R. H. *et. al.*, *Science*, **284**, 1340-1343, 1999.

[27] Kavan L., Rapta P., Dunsch L., Bronikowski M.J., Willis P., Smalley R.E., *J. Phys. Chem* B, **105**, 10764-10771, 2001.

[28] Bozorth R.M., Ferromagnetism, *IEEE Classic Press Reissue*, 440, 2003.

[29] Drings H., Viswanath R. N., Kramer D., Lemier C.,Weissmueller J., Wuerschum R., *Appl. Phys. Lett.*, **88**, 253103, 2006.

[30] Ohno H., Chiba D., Matsukura F., Omiya T., Abe E., Dietl T., Ohno Y., Ohtani K., *Nature*, **408**, 944-946, 2000.

[31] Crespo P., Litran R., Rojas T. C., Fuente J. M. De La, Sanchez-Lopez J. C., Garcia M. A., Hernando A., Penades S., Fernendez A., *Phys. Rev. Lett.*, **93**(8), 087204, 2004.

[32] Weisheit M., Fähler S., Marty A., Souche Y., Poinsignon C., Givord D., *Science*, **315**, 349-350, 2007.

[33] Nash A., Nash P., *Binary Alloy Phase diagrams*, **3**, 2840, 1991.

[34] Ishida K., Nishizawa T., *Binary Alloy Phase Diagrams*, **2**, 1221, 1990.

[35] Ferrando W. A., Segnan R., Schindler A. I., *Phys. Rev.* B, **5**(12), 4657-4664, 1972.

[36] Klug H. P., Alexander L. E., *X-Ray Diffraction Procedures*, Wiley, New York, 1974.

[37] Tracy J. B., Weiss D. N., Dinega D. P., Bawendi M. G., *Phys. Rev.* B, **72**, 064404, 2005.

[38] Punnoose A., Magnone H., Seehra M. S., *Phys. Rev.* B, **64**, 174420, 2001.

[39] Meiklejohn W. H., Bean C. P., *Physical Review*, **102**(5), 1413-1414, 1956.

[40] Persson K., Ersson A., Colussi S., Trovarelli A., Järas S. G., *Appl. Catalysis* B: *Environmental*, **66**, 175-185, 2006.

[41] Schmahl N. G., Eikerling G. F., *Z. Phys. Chem., Neue Folge* (Wiesbaden), **62**, 268, 1968.

[42] Will G. *et. al.*, *J. Appl. Chem.*, **20**, 394, 1987.

[43] Tamura K., Kimura Y., Suzuki H., Kido O., Sato T., Tanigaki T., Kurumada M., Saito Y., Kaito C., *Jpn. J. Appl. Physics.*, **42**(12), 7489-7492, 2003.

[44] Grden M., Klimek K., Czerwinski A., *Electrochimica Acta*, **51**, 2221-2229, 2006.

[45] Grden M., Czerwinski A., Golimowski J., Bulska E., Krasnodebska-Ostrega B., Marassi R., Zamponi S., *J. Electroanal. Chem.*, **460**, 30-37, 1999.

[46] Grden M., Kusmierczyk K., Czerwinski A., *J. Solid St. Electrochem.*, **7**, 43-48, 2002.

[47] http://www.intox.org/databank/documents/chemical/ethylace/cie61.htm.

[48] Trémillon B., *Chemistry in Non-aqueous Solvents*, D. Reidel Publishing Company, Holland, 1974.

[49] Yan Z. C., Zhang Y., Okumura H., Xiao J. Q., Stoyanov S., Skumryev V., Hadji-panayis G. C., *Phys. Rev.* B, **67**, 054403, 2003.

[50] Lemier C., Ghosh S., Weissmueller J., *MRS Res.* Soc. Symp. *Proc.*, 876E, R2.6, 2005.

[51] Ghosh S., Lemier C., Weissmüller J., *IEEE Trans. on Mag.*, **42**(10), 3617-3619, 2006.

[52] Wang Z., Kunkel H. P., Williams G., *Physica* B, **165**(1), 195-196, 1990.

[53] Jamieson H. C., Manchester F. D., *J. Phys. F: Metal Phys.*, **2**, 323-336, 1972.

[54] Viswanath R. N., Krammer D., Weissmüller J., *Langmuir*, **21**, 4604-4609, 2005.

[55] Wicke E., Brodowsky H., *Hydrogen in Metals II*, edited by Alefeld G., Völkl, Springer, Berlin 1978.

[56] Treutmann W., *Z. Angew. Phys.*, **30**, 5, 1970.

[57] Drings H., *Doctoral thesis*, Technische Universität Graz, 2004.

[58] Ibach H., *Physics of Surfaces and Interfaces*, Springer, Berlin, 2006.

[59] Jiles D., *Introduction to Magnetism and Magnetic Materials*, Chapman and Hall, London, 1991.

[60] Nickel, Cobalt, and Their Alloys, *ASM Specialty Handbook*, edited by Davis J. R., Davis & Associates.

[61] Haiss W., *Rep. Prog. Phys.*, **64**(5), 591-648, 2001.

[62] Weissmüller J., Cahn J. W., *Acta Mater.*, **5**(4), 1899-1906, 1997.

[63] Weissmüller J., Kramer D., *Langmuir*, **21**, 4592-4603, 2004.

[64] Weigend F., Evers F., Weissmüller J., *Small*, **2**(12), 1497-1503, 2006.

[65] Nichols R. J., Nouar T., Lucas C.A., Haiss W., Hofer W.A., *Surf. Sci.*, **513**(2), 263-271, 2002.

[66] Beille J., Tournier R., *Phys. F: Metal Phys.*, **6**(4), 621-629, 1976.

[67] Gey W., Köhnlein D., Phys Lett., **29A**(8), 450-451, 1969.

[68] Beille J., Chouteau J., *Phys. F: Metal Phys.*, **5**, 721-731, 1975.

[69] Gugan D., Rowlands G.,*Proc. Phys. Soc.*, **72**, 207-213, 1958.

[70] Gugan D., *Proc. Phys. Soc.*, **72**(6), 1013-1025, 1958.

[71] O'Handley R. C., *Modern Magnetic Materials*, *Principles and Applications*, A Wiley-Interscience Publication, 319.

[72] Jr Brown W. F., Micromagnetics, edited by Marshak R. E., 1963.

[73] Tokunaga T., Tange H. Goto M., *J. Phys. Soc. Japan*, **34**, 1103, 1973.

[74] Fujiwara H., Tokunaga T., *J. Phys. Soc. Japan*, **39**(4), 927-933, 1975.

[75] Fujiwara H., Kadomatsu H., Tokunaga T., *J. Mag. Mag. Mater.*, **31**, 809, 1983.

[76] Gontarz R., Lucinski T., *J. Mag. Mag. Mater.*, **101**, 253-255, 1991.

[77] Gontarz R., Smardz L., Szymanski B., Juzikis P., *J. Mag. Mag. Mater.*, **120**, 278-280, 1993.

[78] Takahashi H., Tsunashima S., Iwata S., Chiyama U. S., *Jpn. J. Appl. Phys.* **32**(2), L1328-L1331, 1993.